An Electrostatic Mechanism Closely Reproducing Observed Behavior in the Bacterial Flagellar Motor

Dieter Walz* and S. Roy Caplan†

*Biozentrum, University of Basel, CH-4056 Basel, Switzerland, and †Department of Biological Chemistry, The Weizmann Institute of Science, 76100 Rehovot, Israel, and Department of Physiology, McGill University, Montreal, Québec H3G 1Y6, Canada

ABSTRACT A mechanism coupling the transmembrane flow of protons to the rotation of the bacterial flagellum is studied. The coupling is accomplished by means of an array of tilted rows of positive and negative charges around the circumference of the rotor, which interacts with a linear array of proton binding sites in channels. We present a rigorous treatment of the electrostatic interactions using minimal assumptions. Interactions with the transition states are included, as well as proton–proton interactions in and between channels. In assigning values to the parameters of the model, experimentally determined structural characteristics of the motor have been used. According to the model, switching and pausing occur as a consequence of modest conformational changes in the rotor. In contrast to similar approaches developed earlier, this model closely reproduces a large number of experimental findings from different laboratories, including the nonlinear behavior of the torque–frequency relation in *Escherichia coli*, the stoichiometry of the system in *Streptococcus*, and the pH-dependence of swimming speed in *Bacillus subtilis*.

GLOSSARY

d_c	distance between the channel axis and the circumference of the rotor
d_m	thickness of rotor (membrane)
$d_{\kappa,\lambda,\nu}$	distance between charge $Q_{\kappa,\lambda,\nu}$ and the position $(x_o, 0, z)$ on the channel axis
e_o	elementary charge
f	frequency of rotation; subscripts br, bt, fl, lf, and mot for body roll, body tethered cell, flagellum, level flow, and motor, respectively
f'_{mot}	dimensionless motor frequency defined in Eq. 33
G°	standard free energy
G_c	free energy due to electrostatic interaction between protons in different channels
G_p	free energy due to electrostatic interaction between protons in the same channel
G_r	free energy due to electrostatic interaction of a proton with the rotor charges
h	Planck's constant
$J_{i,j}$	flow of protons between states i and j of a channel
J_{ex}	flow of protons from the periplasmic space into a channel
$J_{ex,tot}$	total proton flow from the periplasmic space into all channels
J_{in}	flow of protons from the channel into the cytoplasm
$J_{in,tot}$	total proton flow from all channels into the cytoplasm
J_H	proton flow through motor
$K_{i,i+1}$	equilibrium constant of transition between states i and $i + 1$
k	Boltzmann's constant
$k_{subscript}$	proportionality constant (subscripts ext, tor, mot, $\Delta\psi$, v relate to Eqs. 37, 39, 39, 41, 44, respectively)
k_{bt}, k_{br}, k_{fl}	frictional drag coefficients for tethered cell, body roll, flagellum
n	number of channels
P	δ/ϕ (pitch)
p_i	probability of the ith state
pH_{in}, pH_{ex}	pH in the cytoplasm, suspending medium
$Q_{\kappa,\lambda,\nu}$	κth charge on a row in λth repeat with charge number ν
q	number of charges in a row
R	radius of the rotor
r	number of repeats
s	number of proton binding sites in a channel
T	absolute temperature
T_{ref}	reference temperature
T_i	torque generated by the ith state
T_{ch}	torque generated by a single channel
T_{tot}	total torque, generated by all channels
T_{mot}	torque generated by the motor
T_{tor}	torque due to torsion in the hook/filament complex
T_{ext}	external torque exerted on the motor
$T_{ext,r}$	relative external torque exerted on the motor
t	time
U_{ex}	externally applied voltage
x	x-coordinate
x_o	distance between axes of rotor and channel
y	y-coordinate

Received for publication 2 April 1999 and in final form 2 October 1999.

Address reprint requests to Dieter Walz, Biozentrum, University of Basel, Klingelbergstrasse 70, CH-4056 Basel, Switzerland. Tel.: +41-61-267-2224; Fax: +41-61-267-2208; Email: Dieter.Walz@unibas.ch.

© 2000 by the Biophysical Society

0006-3495/00/02/626/26 $2.00

Z_i	charge number of the *i*th proton binding site in a channel
z	*z*-coordinate
z_i	*z*-coordinate of *i*th proton binding site in a channel
$z_i^{\#}$	*z*-coordinate of the *i*th transition state between sites *i* and *i* + 1 in a channel
$\alpha_{i,i+1}$	transition probability per unit time (intrinsic rate constant) for the transition from state *i* to state *i* + 1
$\alpha^*_{i,i+1}$	first order rate constant including the effect of electrostatic interaction, membrane potential, and proton concentration
β_i	relative rate constant of *i*th transition
γ	tilt angle
δ	horizontal angle corresponding to tilt
ϵ_o	permittivity in vacuo
ϵ	relative permittivity
$\zeta_{f,i}$, $\zeta_{b,i}$	dimensionless distances defined in Eqs. B3 and B4
η	viscosity of the medium
θ	rotation angle
κ	transmission coefficient of transition state theory; running index for charges *Q* on a row
λ	running index for repeats on the rotor
μ_H	chemical potential of protons
$\tilde{\mu}_H$	electrochemical potential of protons
ν	charge number of charges *Q* on rotor circumference (± 1)
ν_H	proton stoichiometry (number of protons transferred per revolution)
ρ	rotation angle as a fraction of repeat angle
$\Delta\rho_j$	phase shift of the *j*th channel
ϕ	angle of repeat
$\chi_{\kappa,\lambda,\nu}$, $\chi'_{\kappa,\lambda,\nu}$	angles defined in Fig. 1
$\Delta\psi_m$	membrane potential
$\Delta\psi_{m,0}$	resting membrane potential

INTRODUCTION

The rotary motor responsible for the spinning of a bacterial flagellum is one of the most intriguing of microbiological systems, and it presents a major challenge from the viewpoint of bioenergetics. A flagellum is a complex macromolecular machine that can be divided into three parts: 1) the filament that protrudes from the cell body and has a helical shape, 2) the basal body that is anchored to both the outer cell wall and the cell membrane, and 3) the hook that connects the filament to the basal body (reviewed in Caplan and Kara-Ivanov, 1993; Macnab, 1996). The basal body consists of a central rod and 5 ring-shaped structures. Two rings (L and P) are adjacent to the cell wall and are thought to act as a bushing for the rod. Two rings (M and S) are adjacent to the cell membrane and are thought to constitute the rotor of the motor. The fifth ring (C) is bell shaped, protrudes into the cytoplasm, and is probably built from the components that are responsible for switching (see below). A ring of particles (also called studs or force-generating units) are embedded in the cell membrane around the M ring and are thought to act as the stator of the motor. The MS ring consists of the proteins called FliF and FliG, whereas the particles are formed by the proteins called MotA and MotB. The proteins FliM and FliN, together with a part of FliG, form the C ring.

The flagellar motor is a mechanochemical energy converter. Its driving force is the difference in electrochemical potential of protons, $\Delta\tilde{\mu}_H$, between the periplasmic space (the space between cell wall and cell membrane) and the cytoplasm. The output force is the torque exerted on the filament, and the conjugate flow is the frequency of rotation of the filament with respect to the cell body. Flagella can rotate counterclockwise (CCW) or clockwise (CW) as seen looking from the tip toward the cell body, without a reversal of the driving force. All flagella of a cell rotate in the same direction at any given time. Switching between rotation directions occurs spontaneously, and the switching frequency is modulated by chemotactic agents (reviewed in Eisenbach, 1996). When rotating in CCW mode, the filaments of all flagella are bundled together, and the cell swims linearly with an approximately constant speed. After switching to CW rotation, the flagella fly apart and the cell tumbles. The steady state of rotation after switching is reached within milliseconds, i.e., the inertia of the rotating parts is negligibly small. At steady state, the motor rotates more or less smoothly, although a stepping of the motor can be deduced from the analysis of fluctuations of its frequency (Samuel and Berg, 1995, 1996). These features form the basis for any model of the flagellar motor.

The mechanism of coupling of the transmembrane flow of protons to the rotation of a flagellum is not as yet understood. A wide variety of models of the flagellar motor have been developed in recent years (for a review see, e.g., Caplan and Kara-Ivanov, 1993; Berg and Turner, 1993; Schuster and Khan, 1994). Among these, the two types of mechanism that have been analyzed quantitatively, in terms of what was known about the structure and function of the motor at the time, are those based on fixed elastic elements analogous to muscle cross-bridges (Berg and Khan, 1983; Läuger, 1988; Meister et al., 1989), and those based on electrostatic interaction (Berry, 1993; Doering et al., 1995; Elston and Oster, 1997). Coupling between the linear motion of protons and rotation can be accomplished by means of a helical array of rotor elements interacting with a linear array of stator elements. Helical arrays or tilted rows were suggested both by Läuger (1977) and Macnab (1979). Berry (1993) was the first to consider a purely electrostatic model in which no structural complementarity is required between the rotor and the force-generating units. He assumed the

presence of alternating tilted rows of positive and negative charges around the rotor, and showed that torque can be developed in such a system. Unfortunately, his analysis was over-simplified and led to a number of incorrect and misleading conclusions. However, because Berry's concept is both electrostatically sound and physicochemically convincing, we have used it as the basis of a new model that takes explicit account of the presently known structural and functional aspects of the flagellar motor.

THEORETICAL

Torque balances and sign convention

It has become customary to assign a positive sense of rotation to a flagellum that rotates CCW when viewed from the outside of the cell. Similarly, by convention the externally applied torque T_{ext} causing such a rotation is considered positive. Hence, in the steady state of rotation of a tethered cell

$$T_{mot} + T_{ext} - k_{bt}\eta f_{bt} = 0, \tag{1}$$

where T_{mot} denotes the torque generated by the motor, and f_{bt} is the rotational frequency of the cell body measured in Hz. The frictional drag coefficient of the cell body rotating about a tether is given by k_{bt}, and η denotes the viscosity of the medium. Because T_{mot} represents a torque exerted by the stator on the cell body and by the rotor on the flagellar filament, the torque balance for a freely swimming cell at steady state reads

$$T_{mot} = k_{br}\eta f_{br} = k_{fl}\eta f_{fl} + T_{tor}. \tag{2}$$

Here, f_{br} and f_{fl} denote the body-roll and flagellar (bundle) frequencies, respectively, whereas k_{br} and k_{fl} are the corresponding coefficients relating frictional drag to viscosity. T_{tor} represents torque due to torsion in the hook/filament complex which, as an approximation, may be assumed to be proportional to f_{fl}. The motor frequency f_{mot}, i.e., the rotational frequency of the rotor with respect to the cell body, is related to the different frequencies by

$$f_{mot} = f_{bt} \quad \text{or} \quad f_{mot} = f_{br} + f_{fl} \tag{3}$$

under tethered or swimming conditions, respectively (Caplan and Kara-Ivanov, 1993).

We define positive proton flow to be directed from the extracellular space to the cytoplasm. Accordingly, the positive driving force for protons, i.e., the electrochemical potential difference $\Delta\tilde{\mu}_H$, must also be directed inward. Hence $\Delta\tilde{\mu}_H = \tilde{\mu}_{H,ex} - \tilde{\mu}_{H,in} = \Delta\mu_H + e_o\Delta\psi_m$, where the chemical potential difference $\Delta\mu_H = \mu_{ex} - \mu_{in} = kT \ln 10\,(pH_{in} - pH_{ex})$, and the membrane potential $\Delta\psi_m = \psi_{ex} - \psi_{in}$. Here e_o, k, and ψ denote the elementary charge, Boltzmann's constant, and the electrical potential, respectively, whereas the subscripts ex and in refer to the suspending medium and the cytoplasm, respectively. Note that pH and potential are assumed to be equal in the periplasmic space and in the suspending medium.

Electrostatics

Figure 1 shows a sketch of the rotor, i.e., the MS ring, which is approximated as a disk with radius R and thickness d_m. Two adjacent tilted rows of q charges, one a negative set ($\nu = -1$) and the other a positive set ($\nu = 1$), form a repeat unit. The number of repeats is r, and hence the angle of the repeat unit is

$$\phi = 2\pi/r. \tag{4}$$

The pitch of the rows, P, is defined for our purposes as δ/ϕ, where δ is the angular offset between the top and bottom surfaces of the rotor. The parameter ρ measures the rotation angle θ as the fractional remainder of the quotient θ/ϕ,

$$\rho = \mathrm{rem}(\theta/\phi), \tag{5}$$

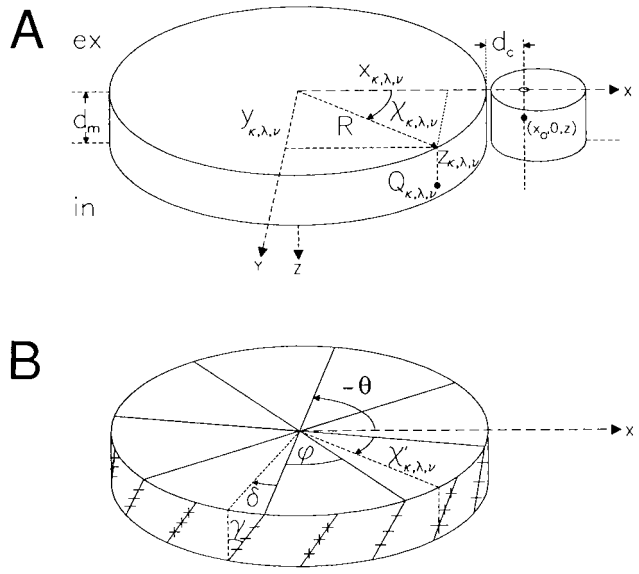

FIGURE 1 Schematic diagrams of the rotor showing the principle geometric parameters, including the alternating tilted rows of positive and negative fixed charges. (*A*) The rotor (radius R, thickness d_m), and one representative force-generating unit containing of a single channel (at a distance d_c from the perimeter of the rotor), are situated within a rectangular Cartesian coordinate system as shown. The rod and hook (not shown), to which the flagellar filament is attached, project up from the center of the rotor in the $-z$ direction, toward the exterior of the bacterium. The coordinates of a particular position in the channel occupied by a proton are depicted, as well as those of a particular fixed charge $Q_{\kappa,\lambda,\nu}$ on the rotor (the κth charge on a row in the λth repeat with charge number ν). (*B*) Eight representative repeat units are illustrated, with the angular position of the selected fixed charge relative to its repeat unit indicated. The angle of repeat is ϕ, the tilt and corresponding horizontal offset angles are γ and δ, respectively, and θ is the angle of rotation.

and varies between 0 and 1. The free energy G_r for a proton at the position $(x_o, 0, z)$ that arises from the electrostatic interaction with all charges $Q_{\kappa,\lambda,\nu}$ on the rotor can be calculated by a linear superposition using Coulomb's law (see Appendix A),

$$G_r(\rho, z) = e_o^2/[4\pi\epsilon_o] \sum_{\kappa=1}^{q} \sum_{\lambda=1}^{r} \sum_{\nu=\pm1} \nu/[\epsilon(d_{\kappa,\lambda,\nu}) d_{\kappa,\lambda,\nu}(\rho, z)]. \quad (6)$$

For reasons to be discussed below, the relative permittivity ϵ is given the argument d to indicate that it is distance dependent.

Kinetics

Most of the data available to test our model were obtained in experiments performed with motors having a full complement of force-generating units, for which average frequencies were determined. Under these conditions, a smooth rotation of the motor is normally seen on all time scales except when measuring fractions of a rotation (Kara-Ivanov et al., 1995). Hence, we can safely ignore Brownian motion and use a deterministic instead of a statistical approach to the kinetics of the system. Because $d\theta/dt = 2\pi f$, it follows from Eqs. 4 and 5 that

$$d\rho/dt = rf. \quad (7)$$

Figure 2 shows a kinetic scheme for the transport of protons through the channel of a force-generating unit. The circles represent binding sites for protons, and are filled if a proton is bound. The number of binding sites s includes two mandatory outer binding sites adjacent to the aqueous phases and any additional inner binding sites that may be present. Let p_i denote the probability of the ith state, then, differentiating the probabilities with respect to time t, we have

$$dp_1/dt = \alpha^*_{2,1}(\rho)p_2(\rho) + \alpha^*_{s+1,1}(\rho)p_{s+1}(\rho) + \alpha^*_{s+2,1}(\rho)p_{s+2}(\rho) - [\alpha^*_{1,2}(\rho) + \alpha^*_{1,s+1}(\rho) + \alpha^*_{1,s+2}(\rho)]p_1(\rho), \quad (8)$$

$$dp_i/dt = \alpha^*_{i-1,i}(\rho)p_{i-1}(\rho) + \alpha^*_{i+1,i}(\rho)p_{i+1}(\rho) - [\alpha^*_{i,i-1}(\rho) + \alpha^*_{i,i+1}(\rho)]p_i(\rho) \quad i = 2, \ldots, s-1, s+1, \quad (9)$$

$$dp_s/dt = \alpha^*_{s-1,s}(\rho)p_{s-1}(\rho) + \alpha^*_{s+1,s}(\rho)p_{s+1}(\rho) + \alpha^*_{s+2,s}(\rho)p_{s+2}(\rho) - [\alpha^*_{s,s-1}(\rho) + \alpha^*_{s,s+1}(\rho) + \alpha^*_{s,s+2}(\rho)]p_s(\rho), \quad (10)$$

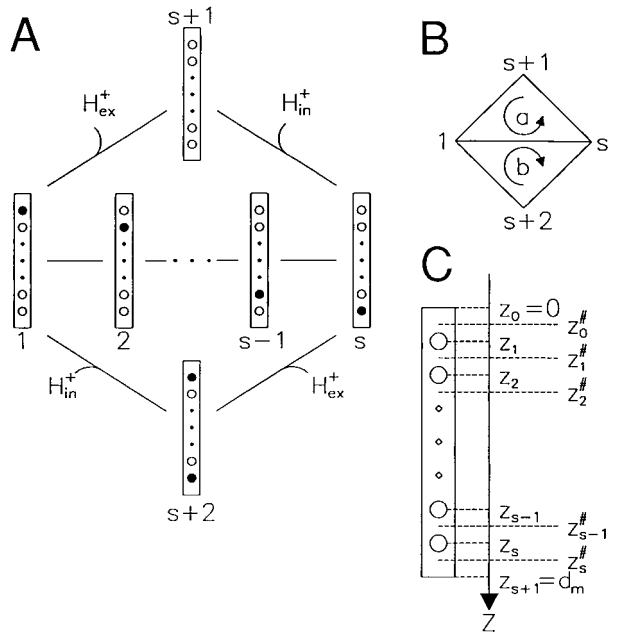

FIGURE 2 Channel kinetics. (*A*) Diagram showing the possible states of the channel following proton binding from, or release to, the periplasmic space or the cytoplasm, and internal proton transitions. Each line represents a forward and backward reaction to which a rate constant is assigned. The channel has s binding sites numbered in sequence from the cell exterior to the cell interior, and each state is labeled by the number of the site occupied. The empty state is designated $s + 1$, and the only state considered having more than one bound proton is designated $s + 2$. (*B*) Schematic cycle diagram showing the two constituent cycles designated a and b, and the sign convention adopted for the cycle fluxes. (*C*) The positions (along the z coordinate) of the ith proton-binding site z_i and the ith transition state $z_i^\#$ in the channel.

$$dp_{s+1}/dt = \alpha^*_{s,s+1}(\rho)p_s(\rho) + \alpha^*_{1,s+1}(\rho)p_1(\rho) - [\alpha^*_{s+1,s}(\rho) + \alpha^*_{s+1,1}(\rho)]p_{s+1}(\rho), \quad (11)$$

$$dp_{s+2}/dt = \alpha^*_{s,s+2}(\rho)p_s(\rho) + \alpha^*_{1,s+2}(\rho)p_1(\rho) - [\alpha^*_{s+2,s}(\rho) + \alpha^*_{s+2,1}(\rho)]p_{s+2}(\rho), \quad (12)$$

$$\sum_{i=1}^{s+2} p_i = 1. \quad (13)$$

As shown in Appendix B, the forward and backward rate constants, $\alpha^*_{i,i+1}$ and $\alpha^*_{i+1,i}$, include intrinsic transition probabilities per unit time, and several factors depending on the electrostatic interaction energies G_r, G_c, and, where appropriate, G_p (cf., Eqs. 6, 26, B16, and B17), the membrane potential $\Delta\psi_m$, and pH_{ex} and pH_{in}. The scheme used here includes $s + 2$ states, although, in principal, it could include many more states. However, as will be discussed below, these states can be omitted here without loss of precision.

Torque generation and proton flow in a single channel

The torque generated by a charge with charge number Z on the channel axis is given by $-Z[\partial G_r/\partial\theta]_{\rho,z}$. The torque T_i generated by the ith state of a channel then becomes

$$T_i(\rho) = -p_i(\rho)\sum_{j=1}^{s}(Z_j + \delta_{i,j})[\partial G_r/\partial\theta]_{\rho,zj}$$

$$i = 1, 2, \ldots, s, s+1, s+2 \quad (14a)$$

$$\delta_{i,j} = 1 \quad \begin{array}{l}\text{if} \quad j = i \quad \text{for} \quad i = 1, 2, \ldots, s, s+1,\\ \text{or if} \quad j = 1, s \quad \text{for} \quad i = s+2\end{array} \quad (14b)$$

$$\delta_{i,j} = 0 \quad \text{for all other cases,}$$

where Z_j denotes the charge number of the jth binding site. Note that the partial derivatives are weighted by the probabilities p_i of the channel states. The partial derivative of G_r with respect to θ is, in view of the sign convention chosen,

$$\left[\frac{\partial G_r}{\partial\theta}\right]_{\rho,z} = \frac{e_o^2 x_o R}{4\pi\epsilon_o}\sum_{\kappa=1}^{q}\sum_{\lambda=1}^{r}\sum_{\nu=\pm1}\nu\sin\chi_{\kappa,\lambda,\nu} \times\frac{d_{\kappa,\lambda,\nu}(\partial\epsilon/\partial d)_{d(\kappa,\lambda,\nu)} + \epsilon(d_{\kappa,\lambda,\nu})}{\epsilon^2(d_{\kappa,\lambda,\nu})d_{\kappa,\lambda,\nu}^3}. \quad (15)$$

The torque associated with a given channel is

$$T_{ch}(\rho) = \sum_{i=1}^{s+2} T_i(\rho). \quad (16)$$

The flow $J_{i,j}$ between states i and j is given by

$$J_{i,j}(\rho) = \alpha_{i,j}^*p_i(\rho) - \alpha_{j,i}^*p_j(\rho). \quad (17)$$

The flows of protons from the periplasmic space into the given channel, J_{ex}, and out of the channel into the cytoplasm, J_{in}, then become

$$J_{ex}(\rho) = [\alpha_{s+1,1}^*(\rho)p_{s+1}(\rho) - \alpha_{1,s+1}^*(\rho)p_1(\rho)] + [\alpha_{s,s+2}^*(\rho)p_s(\rho) - \alpha_{s+2,s}^*(\rho)p_{s+2}(\rho)] \quad (18)$$

$$J_{in}(\rho) = [\alpha_{s,s+1}^*(\rho)p_s(\rho) - \alpha_{s+1,s}^*(\rho)p_{s+1}(\rho)] + [\alpha_{s+2,1}^*(\rho)p_{s+1}(\rho) - \alpha_{1,s+2}^*(\rho)p_1(\rho)]. \quad (19)$$

In general, $J_{ex}(\rho)$ and $J_{in}(\rho)$ are not equal at any given value of ρ. However, the integral of these flows over ρ (from 0 to 1), i.e., the number of protons entering and leaving the channel during a rotation equal to a repeat unit, must be equal.

Channel ensemble

In general, the motor includes n channels, which we arbitrarily number from 1 to n. As is evident from Fig. 3, the value of ρ depends on the geometrical arrangement of the channels and hence, in general, is different for each channel. This is taken into account by assigning a phase shift $\Delta\rho_j$ to the jth channel. The total torque of the motor $T_{tot}(\rho)$ and the total proton flows $J_{ex,tot}(\rho)$ and $J_{in,tot}(\rho)$ generated by the channels then become

$$T_{tot}(\rho) = \sum_{j=1}^{n} T_{ch}(\rho + \Delta\rho_j), \quad (20)$$

$$J_{ex,tot}(\rho) = \sum_{j=1}^{n} J_{ex}(\rho + \Delta\rho_j), \quad (21)$$

$$J_{in,tot}(\rho) = \sum_{j=1}^{n} J_{in}(\rho + \Delta\rho_j). \quad (22)$$

For a symmetric arrangement of channels, we find

$$\Delta\rho_j = \text{rem}[(j-1)r/n]. \quad (23)$$

The averages of T_{tot} and $J_{ex,tot}$ or $J_{in,tot}$ are obtained by integration and yield the motor torque and the proton flow through the motor, respectively,

$$T_{mot} = \int_0^1 T_{tot}(\rho)\,d\rho, \quad (24)$$

$$J_H = \int_0^1 J_{ex,tot}(\rho)\,d\rho = \int_0^1 J_{in,tot}(\rho)\,d\rho. \quad (25)$$

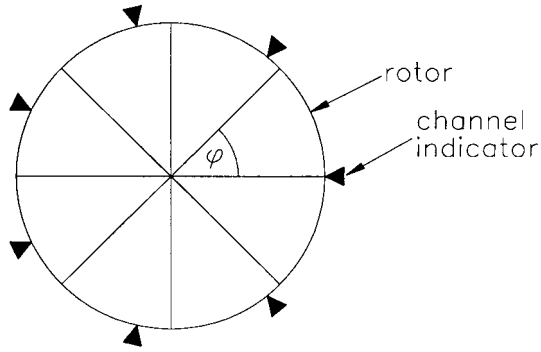

FIGURE 3 Schematic diagram showing a situation in which the number of repeat units constituting the rotor is unequal to an integral multiple of the number of channels, and hence the two are not in register. The channel indicators indicate the positions of a symmetrical array of channels around the rotor.

Another aspect arising from the channel ensemble pertains to the electrostatic interaction between protons in the channels. The free energy G_c for a proton at the position $\{x_o, 0, z\}$ in the channel shown in Fig. 1 *A* that arises from the electrostatic interaction with all protons in the other channels can be calculated by a linear superposition using Coulomb's law (see Appendix A),

$$G_c(\rho, z) = \frac{e_o^2}{4\pi\epsilon_o} \sum_{j=2}^{n} \left[\sum_{i=1}^{s} \frac{p_j(\rho + \Delta\rho_j)}{\epsilon(d_{j,i})d_{j,i}} + p_{s+2}(\rho + \Delta\rho_j)\{[\epsilon(d_{j,1})d_{j,1}]^{-1} + [\epsilon(d_{j,s})d_{j,s}]^{-1}\} \right]. \quad (26)$$

Note that the interaction terms are weighted by the probabilities p_i of the channel states, because the positions of the protons in a channel are only known for a given state.

Numerical computations

It is convenient to scale all rate constants relative to a particular rate constant, and, for this purpose, we choose $\alpha_{2,1}$. Accordingly, making use of the equilibrium constants in Eqs. B14–B17, we write

$$\frac{\alpha_{i+1,i}}{\alpha_{2,1}} = \beta_i \quad \frac{\alpha_{i,i+1}}{\alpha_{2,1}} = K_{i,i+1}\beta_i \qquad i = 1, 2, \ldots, s-1, \quad (27)$$

$$\frac{\alpha_{s,s+1}}{\alpha_{2,1}} = \beta_s \quad \frac{\alpha^o_{s+1,s}}{\alpha_{2,1}} = \beta_s 10^{pK(1,in)}, \quad (28)$$

$$\frac{\alpha_{1,s+1}}{\alpha_{2,1}} = \beta_{s+1} \quad \frac{\alpha^o_{s+1,1}}{\alpha_{2,1}} = \beta_{s+1}\, 10^{pK(1,ex)}, \quad (29)$$

$$\frac{\alpha_{s+2,1}}{\alpha_{2,1}} = \beta_{s+2} \quad \frac{\alpha^o_{1,s+2}}{\alpha_{2,1}} = \beta_{s+2}\, 10^{pK(2,in)}, \quad (30)$$

$$\frac{\alpha_{s+2,s}}{\alpha_{2,1}} = \beta_{s+3} \quad \frac{\alpha^o_{s,s+2}}{\alpha_{2,1}} = \beta_{s+3}\, 10^{pK(2,ex)}. \quad (31)$$

Note that $\beta_1 \equiv 1$. When inserting Eqs. 27–31 into Eqs. 8–12 and dividing the resulting differential equations by $\alpha_{2,1}$, one obtains, by Eq. 7,

$$\alpha_{2,1}^{-1} dp_i/dt = f'_{mot} dp_i/d\rho, \quad (32)$$

where f'_{mot} denotes a dimensionless frequency defined as

$$f'_{mot} = r f_{mot}/\alpha_{2,1}. \quad (33)$$

At static head, i.e., $f'_{mot} = 0$, we get the variables $p_i(\rho)$ as the solution of the system of linear equations derived from Eqs. 8–13 with dp_i/dt set to 0. In the case $f'_{mot} \neq 0$, the differential equations require numerical integration (taking into account Eq. 13), which was performed by the network simulation technique (Walz et al., 1995a). The integration was carried out over two repeats, and only the results from the second repeat were used. Moreover, the results were checked for compliance with the equality on the right hand side of Eq. 25. From the $p_i(\rho)$ values, all other variables can be calculated by means of Eqs. 14–25.

Because the free energy G_c from the interaction of protons in the channels depends on the probabilities p_i of the states (Eq. 26), which, in turn, are also determined by G_c via the rate constants $\alpha^*_{i,j}$ (see Appendix B), an iterative procedure is necessary. The p_i values obtained in a given iteration step were used to calculate G_c for the next step, and the procedure was finished when both T_{mot} and J_H changed less than 1% in the subsequent iteration step.

Adjustment of parameter values was done either manually or, whenever possible, by means of the nonlinear fitting program MODFIT (McIntosh and McIntosh, 1980).

PARAMETERS OF THE MODEL

Electron micrographs prepared by freeze-fracture (Khan et al., 1988) show disk-like structures that are surrounded by a ring of particles exhibiting a diameter of about 5 nm. Both the diameter of the disk and the number of particles vary with species as demonstrated by the values obtained for *Escherichia coli* and *Streptococcus* (Table 1). The diameter of the disk for *Salmonella typhimurium* was deduced from image reconstructions of isolated motor complexes (Sosinsky et al., 1992). The proteins FliF and FliG were found to be present in equimolar ratio and 26 copies of FliF were estimated for the M ring of *S. typhimurium* (see also Macnab, 1996; a somewhat higher but not inconsistent value for FliG was reported by Zhao et al., 1996). Based on these data, we have chosen the values of *R* listed in Table 1 and have calculated the missing values for the number of particles and FliF, FliG by assuming their proportionality to *R*.

Because FliG carries clusters of charged residues (Kihara et al., 1989), which were found essential for torque generation (Lloyd and Blair, 1997) it is reasonable to assume that the lines of charges are associated with this protein. Moreover, the particles were shown to be the MotA/MotB complexes (Khan et al., 1988). It would seem reasonable to set

TABLE 1 Parameters of the model depending on species

	E. coli	*Streptococcus*	*S. typhimurium*
Diameter of disk	20.2 ± 1.9 nm	25.8 ± 2.8 nm	30 nm
Number of particles	11 (10, 12)*	15 (14, 16)*	17†
FliF, FliG	17†	22†	26
R	10 nm	13 nm	15 nm
r	34	44	52
n‡	22	30	34

*Most frequent (minimal, maximal) number observed.
†Calculated by means of proportionality to *R*.
‡Two channels per particle.

r and n equal to the number of FliG subunits and the number of particles, respectively. However, the simulations can reproduce the experimental data only if two repeats per FliG and two channels per MotA/MotB complex are assumed, thus yielding the values for r and n listed in Table 1. For q and P, the smallest values were chosen (Table 2) which yield a sufficiently large torque.

No detailed structural information about the channels in the MotA/MotB particles is yet available. However, motility-deficient mutants indicate that the important part of these channels is the domain formed by α-helices adjacent to the cell membrane (Schuster and Khan, 1994). Hence, we have chosen d_m, which is also the length of the channels, equal to 5 nm, i.e., the average thickness of a biological membrane. Sharp et al. (1995), using tryptophan-scanning mutagenesis of MotA, could not find any typical proton binding sites within the channel and concluded that these sites are most likely provided by water molecules interspersed between the α-helices. Hence, we set the charge number Z_i of all binding sites to 0. We assume the channel axis with the sites to be located close to the boundary of the particles ($d_c = 0.65$ nm) such that an equal spacing of all channels in the particle ring exists. Moreover, we assume an equal spacing of the proton binding sites in a channel, i.e., (Fig. 2 *C*)

$$z_i = id_m/(s+1) \quad i = 0, 1, \ldots, s+1, \tag{34}$$

and a symmetrical barrier for the transition state (Walz and Caplan, 1995),

$$z_i^{\#} = (z_i + z_{i+1})/2, \tag{35}$$

which also yields (Eqs. B3, B4, and 34)

$$\zeta_{f,i} = -\zeta_{b,i} = (z_{i+1} - z_i)/(2d_m) = [2(s+1)]^{-1}. \tag{36}$$

The parameters s, $pK_{1,ex}$, $pK_{1,in}$, $K_{i,i+1}$, G_p, and β_i ($i = 5$–8) are adjusted to yield the best fit to the experimental data. The values for $pK_{2,ex}$, and $pK_{2,in}$ are calculated by means of Eqs. B16 and B17. The equilibrium constants $K_{i,i+1}$ of the inner transitions have to comply with Eq. B18, so only $s - 2$ values for the equilibrium constants need to be adjusted. The relative rate constants β_i for the inner transitions are all set to unity, whereas those for the outer transitions are assumed to be equal but are adjusted. Values for the rate constant $\alpha_{2,1}$ were found to vary considerably even for different cells of the same species under identical conditions. Hence, this parameter is not included in Table 2, but its value will be given in the context of each system to be discussed. Because the geometry of the motor is found to be similar in the investigated species and because there is no evidence for differences in the structure of the MotA/MotB particles of different species, the parameter values listed in Table 2 are taken to be valid for all species.

TABLE 2 Parameters of the model not depending on species

Rotor Parameters		Channel Parameters			
d_m	5 nm	s	5	$K_{1,2}$	9.9
q	6	$pK_{1,ex}$	9.45	$K_{2,3}$	2.7
P	0.5	$pK_{1,in}$	10.5	$K_{3,4}$	0.89
γ*	10.5°	G_p	65.9×10^{-22} J	$K_{4,5}$‖	0.4716
d_c	0.65 nm	$pK_{2,ex}$‡§	8.749	β_i ($i = 1$–4)	1
ϵ/d†	8 nm^{-1}	$pK_{2,in}$‡¶	9.799	β_i ($i = 5$–8)	0.15

*Calculated by means of Eq. A5.
†ϵ proportional to distance d between charges.
‡Depending on temperature, value pertains to 22.6°C.
§Calculated by means of Eq. B16.
¶Calculated by means of Eq. B17.
‖Calculated by means of Eq. B18.

A possible dependence of $pK_{1,ex}$, $pK_{1,in}$, and the equilibrium constants $K_{i,i+1}$ on temperature is not taken into account. Because there is no information available on the effect of temperature on proton binding in the MotA/MotB proteins, any assumption about such a dependence would be purely speculative. Note, however, that $pK_{2,ex}$ and $pK_{2,in}$ are slightly temperature dependent as is evident from Eqs. B16 and B17. In contrast, the rate constants $\alpha_{i,j}$ strongly depend on temperature. This will be treated below, together with the arguments for a temperature independence of the β_i.

Strictly speaking, the use of a relative permittivity (or dielectric constant) ϵ in calculations of electrostatic interactions is legitimate only for macroscopic phases, and its validity on the microscopic level is at least questionable. In fact, the polarizability in macromolecular complexes depends on atoms and bonds, and the electric field in such complexes is influenced by the considerable change in polarizability at the boundaries of the macromolecules that are exposed to water. These effects can be taken into account providing the structure of the complexes is known at the atomic level (Sharp and Honig, 1990). However, experience has shown that, for systems where this information is lacking, a reasonable approximation can be found by means of a relative permittivity whose value depends on the distance between the charges. Both a proportionality to this distance (Harvey, 1989) and an exponential dependence (Elston and Oster, 1997) have been used; we have chosen the former case with a proportionality constant as given in Table 2.

Two additional parameters not pertaining to the model but essential for the simulations are $\Delta\psi_m$ and pH_{in}. Data for *E. coli* at room temperature (Felle et al., 1980), at 30°C (Hirota et al., 1981), and 28°C (Kashket, 1982) are presented in Fig. 4 *A*. It seems that $\Delta\psi_m$ and pH_{in} vary with temperature, but the data are not sufficient to derive a temperature dependence, which therefore was neglected. Khan et al. (1990) reported data for *Streptococcus* (Fig. 4 *B*), whereas Shioi et al. (1980) determined $\Delta\psi_m$ and pH_{in} for *Bacillus subtilis* at 30°C (Fig. 4 *C*). The only data for *S. typhimurium* that could be found in the literature are $\Delta\psi_m \approx 145$ mV for $pH_{ex} = 7$ (Shioi et al., 1982), and $\Delta\psi_m = 162 \pm$

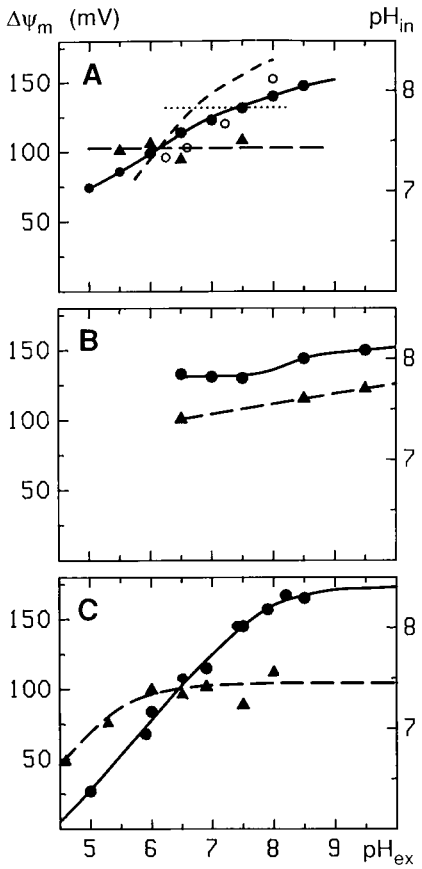

FIGURE 4 Dependence of membrane potential, $\Delta\psi_m$, and pH in the cytoplasm, pH_{in}, on pH in the suspending medium, pH_{ex}, for different species. Experimental data for $\Delta\psi_m$ and pH_{in} are represented by closed circles and triangles, respectively. The solid and long broken lines were drawn through the points and served to determine values for the simulations. (*A*) *E. coli* at room temperature (*closed symbols*, data taken from Felle et al., 1980); *short broken line*, $\Delta\psi_m$ at 30°C (Hirota et al., 1981); *open circles* and *dotted line*, $\Delta\psi_m$ and pH_{in} at 28°C (Kashket, 1982). (*B*) *Streptococcus* at room temperature, data taken from Khan et al. (1990). (*C*) *B. subtilis* at 30°C, data taken from Shioi et al. (1980).

13 mV, $pH_{in} \approx pH_{ex} = 7.5$ (Shioi and Taylor, 1984), both at 30°C. These values are close to those shown in Fig. 4 *A*, so the latter were also used for this species. If not indicated otherwise, values according to the curves drawn through the points in Fig. 4 were used in the simulations.

SIMULATION OF EXPERIMENTAL RESULTS

The analysis of the model yields the torque T_{mot} generated by the motor as a function of the dimensionless frequency f'_{mot}. In experiments, however, only frequencies at the steady state of rotation can be measured. Under this condition, Eqs. 1–3, and 33 can be used to convert the simulated torque–frequency relationship into the form of the experimental data. The values for k_{bt}, k_{br}, k_{fl}, and $\alpha_{2,1}$ are thereby adjusted.

Torque–frequency relationship for tethered cells

When all filaments except one are removed from a bacterial cell and the remaining filament is glued to a support, one obtains what is known as a tethered cell. The rotation frequency of the cell body can then be measured, and an external torque T_{ext} can be applied by means of a rotational electric field. Typical results obtained by Berg and Turner (1993) in such a setup with an *E. coli* cell deficient in switching are shown in Fig. 5. Because it is difficult to calculate the torque exerted by the rotational electric field, T_{ext} is expressed by means of a relative external torque $T_{ext,r}$, such that

$$T_{ext} = k_{ext} T_{ext,r}. \tag{37}$$

If too large a T_{ext} (in either direction) is applied, the motor is irreversibly broken. For such a cell, frequency should be proportional to T_{ext} (cf., Eq. 1 with $T_{mot} = 0$), as shown by the straight line through the origin in Fig. 5 *A*. The slight deviations of the data points from this line indicate that the motor was not fully broken in this case. A fit of these data with a model that includes a factor accounting for the active fraction of the unbroken motor yielded the result shown by the broken line in Fig. 5 *A*. This fraction turned out to be 14%, which may suggest that three channels remained active. The heavy line represents the result of the simulation for an intact motor. It fits the experimental data except for the two points indicated by open symbols. However, these points are most likely not real but artifacts caused by an inhomogeneity in the rotational field (Berry and Berg, 1996). In a case where this artifact is absent, the experimental points are well represented by the simulated curve (Fig. 5 *B*). Moreover, the point on the abscissa of Fig. 5 *A* appears to indicate that the motor opposes clockwise rotation by means of a barrier. Using optical tweezers, however, Berry and Berg (1997) showed that this is not the case.

This behavior of tethered cells in a rotating field appears to be independent of the measuring technique and the species used. Whereas the frequency of the rotating field in the experiments presented in Fig. 5 was set at 2.25 MHz and the field strength was varied by means of the voltage applied to the electrodes, Iwazawa et al. (1993) used frequencies comparable to those of rotating cells and determined the minimal voltage necessary to synchronize cell and field rotation. Their results, obtained with 9 small and 11 large cells, are shown in Fig. 6, together with the simulated curves. The relatively large scatter of the points arises from a considerable variation between cells (see below), which could not have been taken into account because individual cells are not identifiable in the data set. Unfortunately, these authors did not inactivate the motors, and the behavior of the cells under this condition (*thin lines* in Fig. 6) cannot be checked against experimental data. Washizu et al. (1993) applied the same procedure as Berg and Turner (1993) but with six instead of four electrodes and a field frequency of 0.5 MHz.

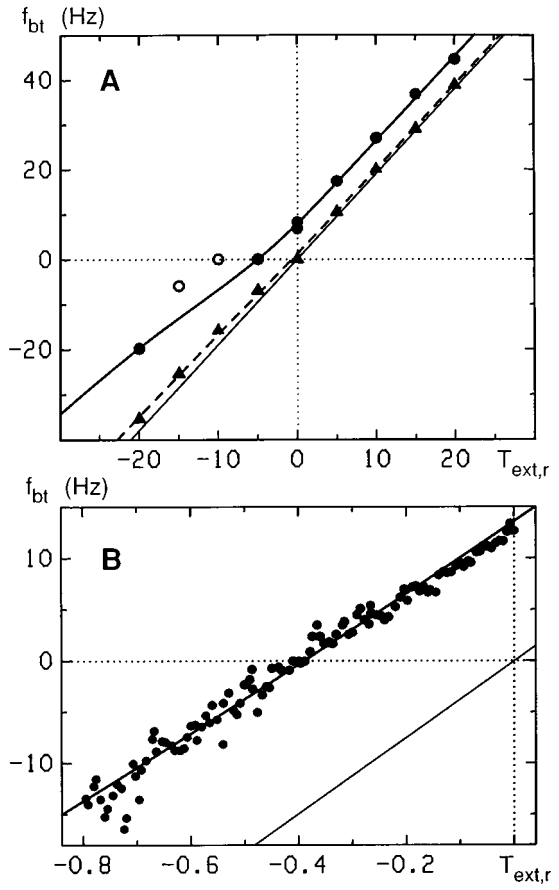

FIGURE 5 Dependence of body rotation frequency, f_{bt}, of tethered *E. coli* cells on externally applied torque. A rotational electric field with variable strength was used to subject the cell body to different torques, which, however, can be given only as a relative quantity $T_{ext,r}$ in arbitrary units. *Circles* and *triangles* represent an intact and an almost fully broken motor, respectively; *open circles* indicate artifactual data. (*A*) Data taken from Fig. 10 of Berg and Turner (1993); temperature 32°C, $pH_{ex} = 7.2$, hence $pH_{in} = 7.43$ and $\Delta\psi_m = 134$ mV (cf. Fig. 4 *A*). (*B*) Data taken from Fig. 6 *b* of Berry and Berg (1996); room temperature, $pH_{ex} = 7$, hence $pH_{in} = 7.43$ and $\Delta\psi_m = 125$ mV (cf. Fig. 4 *A*). In both cases, switching-deficient mutants were used. The curves represent results of simulations with the model using the parameter values listed in Tables 1 and 2. The solid straight lines through the origin indicate the behavior of a fully broken motor. Parameter fitting yielded the following values: $\alpha_{2,1} \times 10^{-5}$ s = 1.1 ± 0.2 and 4.4 ± 0.7, $k_{bt}\eta/(\text{nN·nm·rad}^{-1}\text{·Hz}^{-1}) = 0.112 \pm 0.004$ and 0.075 (manually adjusted because of overparametrization), $k_{ext}/(\text{nN·nm·rad}^{-1}) = 0.213 \pm 0.008$ and 2.79 ± 0.02 for the data in (*A*) and (*B*), respectively. Thus, one arbitrary unit of $T_{ext,r}$ corresponds to 0.21 and 2.8 nN·nm·rad^{-1}, respectively (Eq. 37). The value of the fraction of unbroken motor used when simulating the broken motor data in (*A*) turned out to be 0.14 ± 0.02.

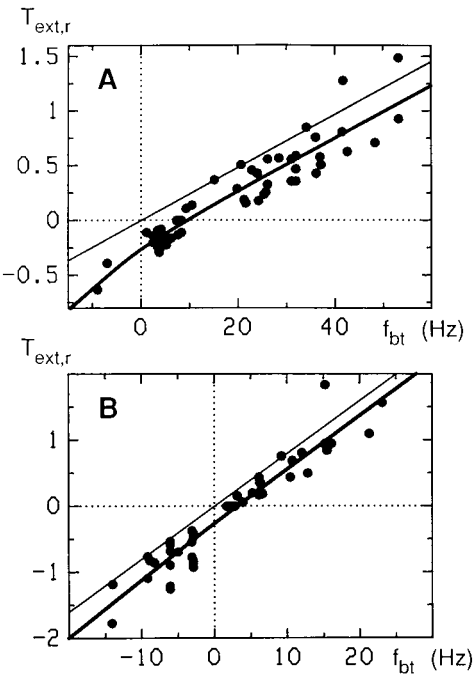

FIGURE 6 Minimal external torque necessary to synchronize cell and field rotation as a function of body rotation frequency f_{bt}. Tethered *E. coli* cells deficient in switching were exposed to a rotational electric field, and $T_{ext,r}$ represents the minimal torque (in arbitrary units), which causes a synchronization of cell body and field rotation. Data points for (*A*) 9 small cells and (*B*) 11 large cells are taken from Fig. 5 of Iwazawa et al. (1993); temperature 25°C, $pH_{ex} = 7$, hence $pH_{in} = 7.43$ and $\Delta\psi_m = 125$ mV (Fig. 4 *A*). The curves represent results of simulations with the model using the parameter values in Tables 1 and 2. The thin straight lines through the origin indicate the behavior of a fully broken motor. Parameter fitting yielded the following values: $\alpha_{2,1} \times 10^{-5}$ s = 1.1 ± 0.6 and 2.0 ± 0.8, $k_{bt}\eta/(\text{nN·nm·rad}^{-1}\text{·Hz}^{-1}) = 0.099 \pm 0.010$ and 0.33 ± 0.03 for the data in (*A*) and (*B*), respectively. The same value for k_{ext} was used for both cases, and the fitting procedure then yielded 4.1 ± 0.5 nN·nm·rad^{-1}.

They used cells of a switching-deficient mutant of *S. typhimurium* and inactivated the motor by ultraviolet (UV) irradiation. The results thus obtained are depicted in Fig. 7, and seem to indicate a slight hysteresis, which, however, was not observed by Berg and Turner (1993) and, most likely, arises from limited experimental accuracy. In this case, too, simulations with the model satisfactorily fit the data and indicate that UV irradiation fully inactivates the motor.

Experiments performed with cells not deficient in switching (Berry et al., 1995) yield results as shown in Fig. 8. It is evident that the dependence of f_{mot} on T_{ext} for CW rotation is centrosymmetrical (around the origin) to that for CCW rotation, which suggests that $T_{mot,CW}(f_{mot}) = -T_{mot,CCW}(-f_{mot})$. Such a relation is achieved in the model by changing the value of P from +0.5 for CCW to −0.5 for CW rotation. The effect of this change in sign on $T_{mot}(f_{mot})$ can be intuitively understood by the following formal operation. If the rotor with a positive value of P is mirror-imaged (Fig. 1) the situation of a rotor with the same but negative value of P is created. The mirror-imaging of the rotor inverts the sign of both the torque and the frequency, which is easily seen if these quantities are represented by vectors that coincide with the rotor axis. The lines in Fig. 8 represent results of simulations with the model using P values with opposite signs. They run through the clouds of

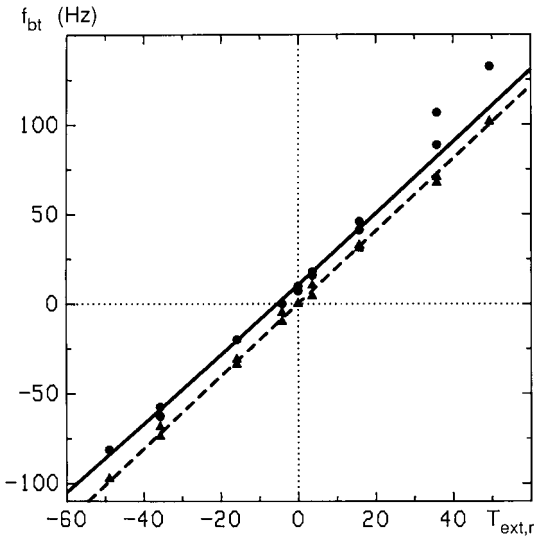

FIGURE 7 Dependence of body rotation frequency, f_{bt}, of tethered *S. typhimurium* cells on externally applied torque. Data are taken from Fig. 7 of Washizu et al. (1993), who used a procedure similar to that mentioned in the legend to Fig. 5. Circles and triangles pertain to an intact and a broken motor, respectively. Because neither temperature nor pH of the medium is given by the authors, usual laboratory conditions were assumed, i.e., 23°C and $pH_{ex} = 7$, hence $pH_{in} = 7.43$ and $\Delta\psi_m = 125$ mV (Fig. 4 *A*). The curves represent results of simulations with the model using the parameter values in Tables 1 and 2. Moreover, parameter fitting yielded $\alpha_{2,1} = (1.4 \pm 0.7) \times 10^6\ s^{-1}$, $k_{bt}\eta = 0.24 \pm 0.02$ nN·nm·rad^{-1}·Hz^{-1}, and $k_{ext} = 0.49 \pm 0.04$ nN·nm·rad^{-1}. In this case, the fitting procedure assigned a value of -0.003 ± 0.062 to the fraction of unbroken motor, which can be interpreted as a fully broken motor.

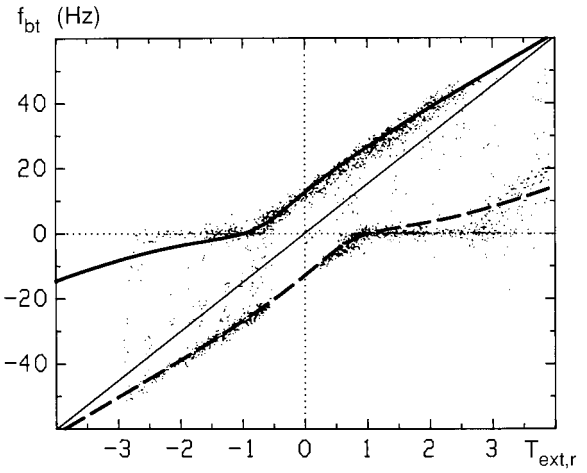

FIGURE 8 Body rotation frequency f_{bt} of a tethered *E. coli* cell not deficient in switching as a function of external torque. Data points for a single cell, which were obtained by the technique mentioned in the legend to Fig. 5, are taken from Fig. 2 *b* of Berry et al. (1995); room temperature and $pH_{ex} = 7$, hence $pH_{in} = 7.43$ and $\Delta\psi_m = 125$ mV (Fig. 4 *A*). The solid and broken lines represent simulations of counterclockwise and clockwise rotation, respectively, while the solid straight line through the origin indicates the behavior of a fully broken motor. They were calculated with the parameter values in Tables 1 and 2, and the following fitted values of the additional parameters: $\alpha_{2,1} = (2.4 \pm 0.2) \times 10^4\ s^{-1}$, $k_{bt}\eta = 0.072 \pm 0.001$ nN·nm·rad^{-1}·Hz^{-1}, and $k_{ext} = 1.09 \pm 0.03$ nN·nm·rad^{-1}.

experimental points except for the artifactual data discussed above. Switching can thus be envisaged as a concerted conformational change of all FliG proteins, most likely together with the FliM and FliN proteins, which causes a flipping of the tilt angle γ (see Appendix A) between $+10°$ and $-10°$.

According to Eq. 1, $T_{ext} = k_{bt}\eta f_0$ for a broken motor, which, upon substitution into Eq. 1, yields (Eq. 3)

$$\Delta f(f_{mot}) = f_{bt} - f_0 = T_{mot}(f_{mot})/(k_{bt}\eta), \qquad (38)$$

where f_{bt} and f_0 denote the frequency of a tethered cell with an intact and a broken motor, respectively, at a given value of T_{ext}. Data calculated according to Eq. 38 by Berg and Turner (1993) are shown in Fig. 9 for different *E. coli* cells at different temperatures. It is important to note that only the data in Fig. 9, *A* and *B* were used to adjust the values of the parameters *s*, $pK_{1,ex}$, $pK_{1,in}$, $K_{i,i+1}$, and G_p. This yielded the data listed in Table 2, which were used for all simulations. The adjustment of the parameters β_i ($i = 5$–8) was not very precise because values in the range of 0.1 to 0.25 with essentially the same values for the parameters $pK_{1,ex}$, $pK_{1,in}$, $K_{i,i+1}$, and G_p yielded equally good fits to the data. However, the simulations of the swimming speed of *B. subtilis* (see below) turned out to be very sensitive to a variation of β_i, and the value listed in Table 2 was obtained by adjustment to these data.

A number of interesting features of the model become evident when comparing the experimental data with the simulated results. 1) Channels with only three or four binding sites (i.e., $s = 3$ or 4) yielded an f_{mot}-dependence of Δf with a steep drop at small f_{mot} values, followed by a maximum above the data points rather than a plateau before it linearly declines along with the data points. Moreover, simulations with $s = 3$ or 4 failed to reproduce the swimming speed of *B. subtilis* (see below). In contrast, the plateau region is substantially shortened with $s = 6$, indicating that $s = 5$ is most likely the appropriate choice. 2) The motor torque of tethered *E. coli* cells rotating at a frequency of 15 Hz was estimated to range between 0.8 and 1.3 nN·nm·rad^{-1} (Blair and Berg, 1988; Braun et al., 1999). The model yields the correct value $T_{mot} = k_{bt}\eta\Delta f \approx 0.9$ nN·nm·rad^{-1} (Eq. 38 and Fig. 9) only if two channels per MotA/MotB particle and two repeats per FliG are assumed, which is the reason for $r = 34$ and $n = 22$ (Table 1). 3) A considerable variation in the dependence of Δf on f_{mot} was found for different cells under identical experimental conditions (Fig. 9), which can be fully accounted for in the model by appropriate values of the rate constant $\alpha_{2,1}$.

Freely swimming cells

By means of optical techniques, Lowe et al. (1987) were able to measure the bundle frequency f_{fl} and the body roll

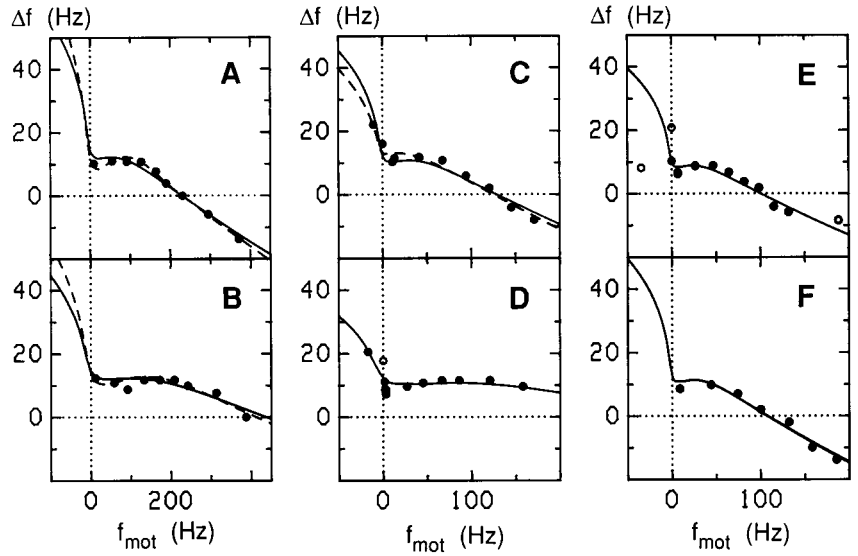

FIGURE 9 Torque-frequency relations for counterclockwise rotation of *E. coli* motors at different temperatures. Data for the frequency difference Δf (Eq. 38) are taken from different figures in the paper of Berg and Turner (1993), whose numbers are given in brackets following the temperatures listed below. Artifactual data (Fig. 5) or data pertaining to a partially broken motor are marked by open symbols. According to Eq. 38, Δf is proportional to T_{mot}. The solid lines represent results of simulations with the model using the parameter values in Tables 1 and 2. For all experiments $pH_{ex} = 7$, hence $pH_{in} = 7.43$ and $\Delta\psi_m = 125$ mV (Fig. 4 *A*). Temperatures and values of $\alpha_{2,1}$ (in 10^4 s^{-1}) and $k_{bt}\eta$ (in nN·nm·rad^{-1}·Hz^{-1}) obtained by parameter fitting are as follows: (*A*) 22.6°C [14 *b*] 8.5 ± 0.3 and 0.075 ± 0.004; (*B*) 22.6°C [14 *c*] 16 ± 1 and 0.074 ± 0.005; (*C*) 16.2°C [13 *b*] 4.6 ± 0.4 and 0.089 ± 0.007; (*D*) 16.2°C [15 *b*] 12 ± 3 and 0.096 ± 0.008; (*E*) 11.2°C [13 *a*] 3.5 ± 0.2 and 0.113 ± 0.010; (*F*) 11.2°C [14 *a*] 3.6 ± 0.2 and 0.103 ± 0.007. The broken lines in (*A*) and (*B*) represent results of simulations with the model using an exponential dependence of the relative permittivity on the distance *d* between charges, $\epsilon = \epsilon(0)\exp\{\lambda d\}$, where $\epsilon(0)$ and λ denote the relative permittivity at zero distance and the reciprocal electric screening distance, respectively. Parameter values as before, except for the following parameters whose values are, for (*A*) and (*B*), respectively: $\epsilon(0) = 3.36$ and 3; $\lambda/nm^{-1} = 0.25$ and 0.5; $pK_{1,ex} = 11.55$ and 9.67; $pK_{1,in} = 12.4$ and 10.65; $G_p \times 10^{22}$ $J^{-1} = 113$ and 85.8; $K_{1,2} = 8.66$ and 8.1; $K_{2,3} = 3.04$ and 2.9; $K_{3,4} = 0.74$ and 0.78; $K_{4,5} = 0.3634$ and 0.5212; $\alpha_{2,1} \times 10^{-4}$ s = 8.2 ± 0.2 and 14.7 ± 0.5; $k_{bt}\eta$/(nN·nm·rad^{-1}·Hz^{-1}) = 0.070 ± 0.003 and 0.066 ± 0.002. The broken line in (*C*) represents the result of a simulation with the model where the free energy $G_c(\rho, z)$ due to interaction between protons in different channels was neglected. Parameter values as before except for the following parameters whose values are $pK_{1,ex} = 8.28$; $pK_{1,in} = 9.4$; $G_p = 53.8 \times 10^{-22}$ J; $K_{1,2} = 7.9$; $K_{2,3} = 2.25$; $K_{3,4} = 1.16$; $K_{4,5} = 0.6393$; $\beta_i = 0.31$ ($i = 5 - 8$); $\alpha_{2,1} \times 10^{-4}$ s = 3.4 ± 0.3; $k_{bt}\eta$/(nN·nm·rad^{-1}·Hz^{-1}) = 0.088 ± 0.008.

frequency f_{br} in suspensions of freely swimming *Streptococcus* cells from three different cultures. A large range of frequencies could be covered by varying the viscosity of the medium. They determined the motor frequency f_{mot} (Eq. 3) and the torque T_{mot} from f_{br} (Eq. 2) by means of a calculated value for k_{br}. As is evident from Fig. 10, both the dependence of frequencies on fluidity, i.e., η^{-1}, and of T_{mot} on f_{mot}, vary with culture. Although the former variation could be explained by differences in k_{fl} and k_{br}, the latter variation cannot. Hence, the quantity most probably responsible is $\Delta\psi_m$. Using $\Delta\psi_m$ as an adjustable parameter, the experimental data can be well represented by the model, as indicated by the curves in Fig. 10, except for the points for tethered cells (*open symbols* in Fig. 10 *B*). But, as mentioned by the authors, these data could have an uncertainty of up to 50% and thus should not be taken as contradictory evidence. When analyzing the data for $f_{fl}(\eta^{-1})$ by means of Eq. 2, the relation $T_{tor} = k_{tor}f_{fl}$ was assumed to hold. The analysis revealed that $k_{tor}\eta^{-1} \ll k_{fl}$, hence,

$$k_{mot} \approx (1/k_{fl} + 1/k_{br})^{-1}, \tag{39}$$

which is the frictional drag coefficient relating T_{mot} to f_{mot}. By Eq. 39, we then find $k_{mot} = 3$ pN·nm·rad^{-1}·Hz^{-1}·cP^{-1}.

Meister et al. (1987) measured the proton flow J_H together with the motor frequency f_{mot} and torque T_{mot} in artificially energized *Streptococcus* cells. They incubated starved cells at pH 8.5 and 200 mM KCl in the presence of valinomycin, and then rapidly transferred them to pH 6.5 and 5 mM KCl by appropriate dilution of the medium. Varying the incubation time before measurements yielded different values of $\Delta\tilde{\mu}_H$ and thus of f_{mot}. Alternatively, f_{mot} was varied by different temperatures or by deuterium substitution. In all three cases, they found J_H to be proportional to f_{mot} within experimental error. The authors therefore concluded that the motor is tightly coupled. The stoichiometry ν_H, i.e., the number of protons passing through the channels per revolution of a flagellum, can be calculated as the ratio J_H/f_{mot}. The values thus found for the three cases were 1440 ± 130, 970 ± 90, and 1310 ± 150, respectively, which yields an average value of 1240 ± 240. The relatively low value obtained with temperature variation is caused by a deviation of the data points for 28°C and 32°C (cf., Fig. 3 in Meister et al., 1987, and Fig. 14 *C*). Simulations with values of $\Delta\psi_m$ and pH_{in} for a fully energized cell (see Fig. 4 *B*) indeed show a proportionality between J_H and f_{mot}, and hence a constant ν_H of 1303 over a large range of f_{mot} (Fig.

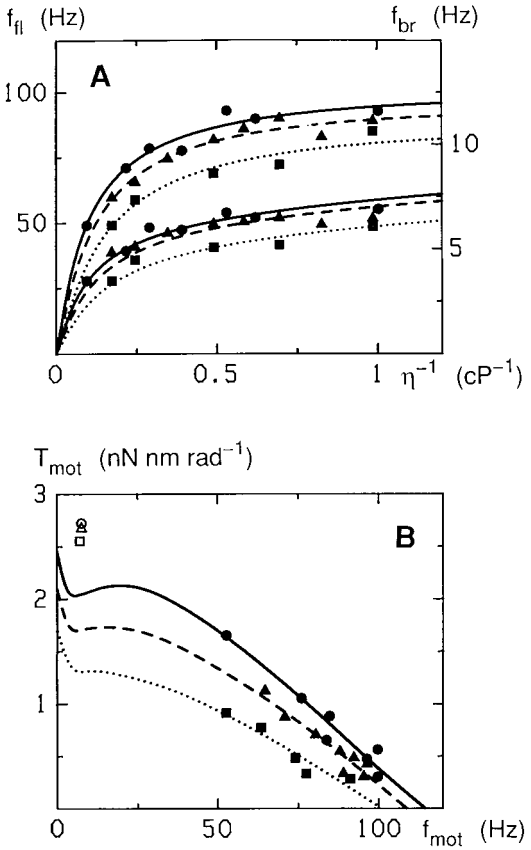

FIGURE 10 (*A*) Dependence of bundle frequency, f_{fl}, and body roll frequency, f_{br}, on fluidity of the medium, and (*B*) torque–frequency relations for freely swimming *Streptococcus* cells. Data for the bundle frequency are taken from Fig. 2 *a* of Lowe et al. (1987). They were measured with cells from three different cultures, as indicated by different symbols, and are plotted in the upper part of (*A*) using the left ordinate. Corresponding values for the body roll frequency were recalculated by means of Eq. 2 from the data shown in (*B*), which were taken from Fig. 3 of Lowe et al. (1987). They are plotted in the lower part of (*A*) using the right ordinate. The average values (in pN·nm·rad^{-1}·Hz^{-1}·cP^{-1}) $k_{fl} = 3.25 \pm 0.05$ and $k_{br} = 44.1 \pm 1.6$ emerged from this recalculation. Temperature 22°C and $pH_{ex} = 7.5$, hence $pH_{in} = 7.5$ (Fig. 4 *B*). The curves represent results of simulations with the model using the parameter values in Tables 1 and 2. Parameter fitting, which, in this case, included $\Delta\psi_m$, yielded the following values for the three cultures represented, respectively, by solid, broken, and dotted lines: $\alpha_{2,1} \times 10^{-4}$ s = 5.5 ± 0.6, 6.5 ± 0.8, and 8.1 ± 1.5; k_{br}/(pN·nm·rad^{-1}·Hz^{-1}·cP^{-1}) = 45 ± 12, 45 ± 12, and 47 ± 10; $\Delta\psi_m$/mV = 156 ± 10, 133 ± 9, and 110 ± 9. Essentially the same value k_{fl} = 3.1 ± 0.2 pN·nm·rad^{-1}·Hz^{-1}·cP^{-1} was found for all cultures. The relation $T_{tor} = k_{tor} f_{fl}$ was assumed to hold. It then appeared from the parameter fitting that the contribution of T_{tor} is rather small, and only one value k_{tor} = 0.4 ± 1.2 pN·nm·rad^{-1}·Hz^{-1} for all cultures could be fitted.

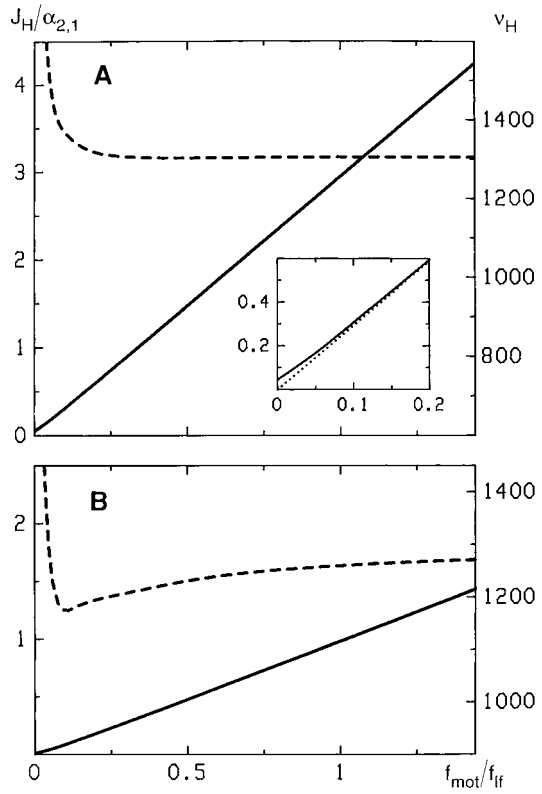

FIGURE 11 Proton flow J_H and proton stoichiometry ν_H as a function of motor frequency f_{mot} for *Streptococcus* cells. Proton flows were simulated with the model, using the parameter values in Tables 1 and 2. Normalized values $J_H/\alpha_{2,1}$ are plotted as a function of the normalized frequency f_{mot}/f_{lf} (*solid lines*), where f_{lf} denotes f_{mot} at level flow, i.e., at $T_{mot} = 0$. The corresponding proton stoichiometries ν_H (*broken lines*) were calculated as $J_H/f_{mot} = J_H \alpha_{2,1}^{-1} r/f'_{mot}$ (Eq. 33). The inset of (*A*) is a blow up of the lower left corner. The dotted line indicates the proportionality between $J_H/\alpha_{2,1}$ and f_{mot}/f_{lf} according to $\nu_H = 1303$. Temperature 24°C; (*A*) $pH_{ex} = 7$, hence $pH_{in} = 7.45$ and $\Delta\psi_m = 132$ mV (Fig. 4 *B*); (*B*) $pH_{ex} = 7.02$, $pH_{in} = 7.62$, and $\Delta\psi_m = 45$ mV, calculated as described in the text.

11 *A*). But a small residual J_H at $f_{mot} = 0$ persists (*inset*, Fig. 11 *A*), which indicates that the motor model is highly but not fully coupled. As a consequence, ν_H approaches infinity if f_{mot} vanishes.

Because, in the case of an incompletely coupled motor, ν_H can be affected by a variation in $\Delta\psi_m$ and pH_{in}, values for these quantities under the experimental conditions were estimated as follows. Providing $pH_{in} = pH_{ex} = pH_\infty$ at the end of the experiment where pH_{ex} is constant, and if constant buffer capacities in the cell and the suspending medium are assumed, pH_{in} at any given pH_{ex} can be calculated as

$$pH_{in} = pH_{in}(0) + \frac{[pH_\infty - pH_{in}(0)][pH_{ex} - pH_{ex}(0)]}{pH_\infty - pH_{ex}(0)}. \quad (40)$$

Here, $pH_{in}(0)$ and $pH_{ex}(0)$ indicate the pH values just after dilution. With $pH_{in}(0) = 8.5$, $pH_{ex}(0) = 6.5$ (see above) and $pH_\infty = 7.245$ (cf., Fig. 1 *A* in Meister et al., 1987), $pH_{in} = 7.62$ is obtained at $pH_{ex} = 7.02$, which is the pH value 48 s after dilution where an experiment was started. The corresponding $\Delta\psi_m$ value was adjusted such that the simulations reproduced the measured T_{mot} value, which yielded $\Delta\psi_m \approx$ 45 mV. As is evident from Fig. 11 *B*, J_H is still about proportional to f_{mot} in this case. But ν_H is no longer constant and varies between 1170 and 1270. In contrast, at $pH_{ex} =$

6.79 (the pH value 22 s after dilution), $pH_{in} = 8.01$ and $\Delta\psi_m \approx 50$ mV are estimated, and the simulations yield a picture similar to that shown in Fig. 11 *A* with $\nu_H = 1300$. This dependence of ν_H on $\Delta\psi_m$ and pH_{in} could explain the deviation of the data points at temperatures above 24°C because the relatively large J_H at these temperatures could have caused an even lower pH_{in} value and a smaller $\Delta\psi_m$.

Immobilized cells with imposed membrane potential

Kami-ike et al. (1991) immobilized *S. typhimurium* cells by pulling them part of the way into glass micropipettes, and monitored the flagellar rotation by optical techniques. They applied voltage pulses U_{ex} between the microelectrode and the suspending medium, and observed a roughly linear dependence of the motor frequency on U_{ex}. Because fully energized cells were used, U_{ex} caused a hyper- or depolarization of $\Delta\psi_m$ around the resting potential $\Delta\psi_{m,0}$. Rather large voltages as compared to $\Delta\psi_{m,0}$ had to be applied because the seal between cell and micropipette had a low resistance. It is reasonable to assume that the change in membrane potential is proportional to the applied voltage, i.e.,

$$\Delta\psi_m - \Delta\psi_{m,0} = k_{\Delta\psi} U_{ex}. \qquad (41)$$

If we further neglect a possible effect of U_{ex} on pH_{in}, the model can well simulate these data, as shown in Fig. 12 *A*. When fitting the parameters $\alpha_{2,1}$, $k_{\Delta\psi}$, $k_{fl}\eta$, and $\Delta\psi_{m,0}$, a value had to be assigned to one of them because, otherwise, the system was overparameterized. We have chosen $k_{fl}\eta = 3$ pN·nm·rad^{-1}·Hz^{-1} as found for *Streptococcus* cells at $\eta \approx 1$ cP, but it should be added that this value is not very crucial. Choosing different values for $k_{fl}\eta$ in the range of 1.5 to 8 yielded equally good fits of the data with a less than 10% variation for the values of the fitted parameters.

Fung and Berg (1995) have considerably improved this technique so that they could calculate the actual membrane potential arising from the applied (or command) voltage. They used cells of an *E. coli* mutant that is devoid of the $F_0F_1H^+$-ATPase and forms polyhooks instead of filaments. The polyhooks were decorated with markers for better detection of rotation which, however, caused higher frictional drags and concomitantly lower rotation frequencies than in the case of filaments. The authors found that fully deenergizing the cells causes not only an arrest of rotation but also a delay in its restart after applying a properly polarized command voltage. Because of this inactivation of torque-generating elements, the experiments were performed only with command voltages that do not lead to complete deenergization. We have found that these experiments can be well simulated (Fig. 12, *B–D*) only if we assume a small difference between pH_{in} and pH_{ex}, which, in the case of completely deenergized cells, is compensated by a Donnan

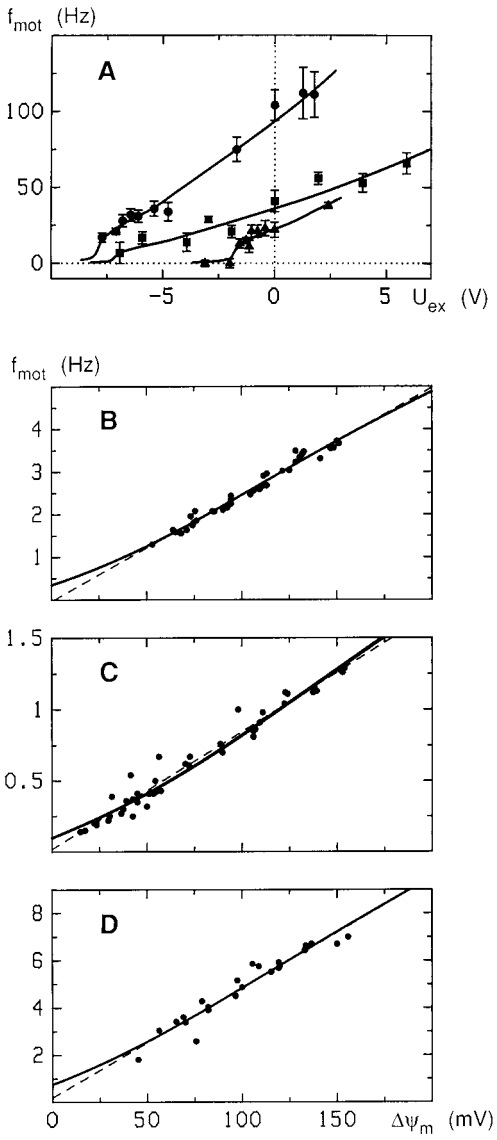

FIGURE 12 Dependence of motor frequency f_{mot} on imposed membrane potential for immobilized cells. (*A*) Data for three *S. typhimurium* cells were taken from Fig. 4 of Kami-ike et al. (1991). For each cell and each value of the externally applied voltage U_{ex}, average values of f_{mot} were calculated, taking into account the standard deviations given by the authors. Room temperature and $pH_{ex} = 6.9$, hence $pH_{in} = 7.43$. The curves represent results of simulations with the model using the parameter values in Tables 1 and 2. The value 3 pN·nm·rad^{-1}·Hz^{-1} was assigned to $k_{fl}\eta$, and the membrane potential $\Delta\psi_m$ was calculated by means of Eq. 41. Parameter fitting yielded the following values for the cells represented, respectively, by circles, squares, and triangles: $\alpha_{2,1} \times 10^{-4}$ s = 4.7 ± 1.1, 1.9 ± 0.2, and 3.4 ± 1.3; $\Delta\psi_{m,0}$/mV = 139 ± 26, 127 ± 6, and 53 ± 17. The value $k_{\Delta\psi} = 0.014 \pm 0.005$ was obtained for all cells. (*B–D*) Data for three *E. coli* cells taken from Fig. 4 of Fung and Berg (1995). Temperature 22°C and $pH_{ex} = 7$; pH_{in} was assumed to be 7.43 for (*B*) and (*D*), and 7.3 for (*C*). The solid lines represent results of simulations with the model using the parameter values in Tables 1 and 2. Parameter fitting yielded the following values for the three cells in (*B*), (*C*), and (*D*), respectively: $\alpha_{2,1} \times 10^{-4}$ s = 3.8 ± 1.0, 2.4 ± 0.8, and 11.5 ± 8.6; $k_{dp}\eta$/(nN·nm·rad^{-1}·Hz^{-1}) = 0.31 ± 0.01, 0.84 ± 0.03, and 0.16 ± 0.01, where k_{dp} denotes the frictional drag coefficient for decorated polyhooks. The broken lines were calculated by linear regression of the data.

potential, thus causing $\Delta\tilde{\mu}_H$ to be zero. The simulated curves in Fig. 12, *B–D* then indicate a finite value of f_{mot} at $\Delta\psi_m = 0$ which, however, may not be observed experimentally because the torque-generating elements are most likely inactivated under this condition.

Effect of temperature

A change in temperature alters the frictional drags because of the temperature dependence of the viscosity η (Eq. 2). It also affects the proton transport kinetics via the exponential terms comprising kT in the expressions for the rate constants (see Appendix B) and due to the temperature dependence of the intrinsic rate constants $\alpha_{i,j}$. Because these rate constants were scaled (Eqs. 27–31), the temperature dependence of $\alpha_{2,1}$ and the β_i has to be investigated. As explained in Appendix B, $\alpha_{2,1}$ is determined by the activation energy $\Delta G_1^{\#} = G^{\circ}(z_2) - G^{\circ}(z_1^{\#})$, and, according to the transition state theory (Glasstone et al., 1941),

$$\alpha_{2,1} = (\kappa kT/h)\exp\{-\Delta G_1^{\#}/(kT)\}. \quad (42)$$

Here, h is Planck's constant, and κ is called the transmission coefficient, which, in biological systems, invariably lies between 0.5 and 1 (Voet and Voet, 1995). The activation energy itself may depend on temperature according to

$$\Delta G_1^{\#} = \Delta G_1^{\#}(T_{ref}) + (T - T_{ref})\partial\Delta G_1^{\#}/\partial T, \quad (43)$$

where T_{ref} denotes a reference temperature. This linear Taylor expansion seems legitimate in view of the relatively small temperature interval covered by the experiments. If Eqs. 27–31 are rewritten in terms of Eq. 42, it is seen that the β_i for inner transitions, whose values are set to unity, are temperature independent, whereas those for outer transitions, whose values were adjusted to 0.15 at 22.6°C, can only be very weakly dependent on temperature.

The effect of temperature on the frictional drag is evident from the values of $k_{bt}\eta$ determined for the experiments presented in Fig. 9. If η of the medium is approximated by that of water, i.e., 1.2643, 1.1054, and 0.9446 cP at 11.2, 16.2, and 22.6°C, respectively, $k_{bt}\eta$ is indeed found to be proportional to η with $k_{bt} = 0.080 \pm 0.002$ nN·nm·rad^{-1}·Hz^{-1}·cP^{-1}. Berg and Turner (1993) have calculated average values for the level flow frequency f_{lf} at $T_{mot} = 0$ (i.e., the intercept of Δf on the abscissa in Fig. 9) for different cells at a given temperature. They found 92.5 ± 13.8 Hz for 28 cells, 138.4 ± 22.1 Hz for 40 cells, and 286.9 ± 53.6 Hz for 41 cells at 11.2, 16.2, and 22.6°C, respectively. The corresponding f'_{mot} values emerging from the simulations are 0.1156, 0.1112, and 0.1043. If the values for $\alpha_{2,1}$, calculated by means of Eq. 33 from these data, are fitted to Eqs. 42 and 43 with κ set to unity, the values listed in Table 3 (row 1) are obtained.

Iwazawa et al. (1993) have measured f_{mot} and T_{mot} of freely swimming *E. coli* cells at different temperatures and found an approximately linear dependence of both quantities on T. An analysis of these data in terms of the model is presented in Fig. 13. The major effect of T is on $\alpha_{2,1}$, as expressed by Eqs. 42 and 43 with an activation energy listed in Table 3 (row 2). The variation of $k_{mot}\eta$ with temperature (*broken lines* in Fig. 13 *B*) is relatively small. Similarly, the torque–frequency relationships per se are only weakly affected by the kT comprising terms in the rate constants. The plateau levels are somewhat decreased with increasing temperature (Fig. 13 *B*), whereas the linearly declining parts are essentially parallel in a plot of T_{mot} versus f'_{mot}. However, in the plot of T_{mot} versus f_{mot} shown in Fig. 13 *B*, these parts are extended toward higher frequencies and their slopes decrease with increasing temperature because of $\alpha_{2,1}$ (Eq. 33), which leads to the strong temperature dependence of f_{mot} for freely swimming cells. Iwazawa et al. (1993) have also measured the body frequency of tethered cells and found a weaker dependence of f_{bt} on temperature (*triangles* in Fig. 13 *A*). Inspection of Fig. 13 *B* reveals the reason for this phenomenon. Because k_{bt} is about 80 times larger than k_{mot}, the lines representing frictional drag (not shown) intersect the torque–frequency curves in the plateau region, which is considerably less affected by temperature than the linear declining parts.

The analysis described above was also applied to data for freely swimming *Streptococcus* cells that were either fully energized (Lowe et al., 1987) or artificially energized (Meister et al., 1987). The corresponding activation energies are listed in Table 3 (rows 3 and 4). As in the case of *E. coli* cells, the linear dependence of f_{mot} on temperature observed by the authors is only an approximation (Fig. 14, *A* and *B*). In fact, if this dependence were strictly linear, one would expect that flagellar rotation ceases at low temperatures or even reverses direction, which is clearly not the case

TABLE 3 Activation energy $\Delta G_1^{\#}$ for the transition between states 1 and 2

Species	$\Delta G_1^{\#}(T_{ref})$* (10^{-22} J)	$\partial\Delta G_1^{\#}/\partial T$ (10^{-22} J·K^{-1})	Experimental Conditions
E. coli	734 ± 1	−1.4 ± 0.2	Fully energized tethered cells with T_{ext}
E. coli	762 ± 1	0.48 ± 0.06	Fully energized freely swimming cells
Streptococcus	751 ± 1	0.19 ± 0.14	Fully energized freely swimming cells
Streptococcus	766 ± 1	−0.73 ± 0.18	Artificially energized freely swimming cells

*Reference temperature T_{ref} = 295.15 K (22°C), transmission coefficient $\kappa = 1$.

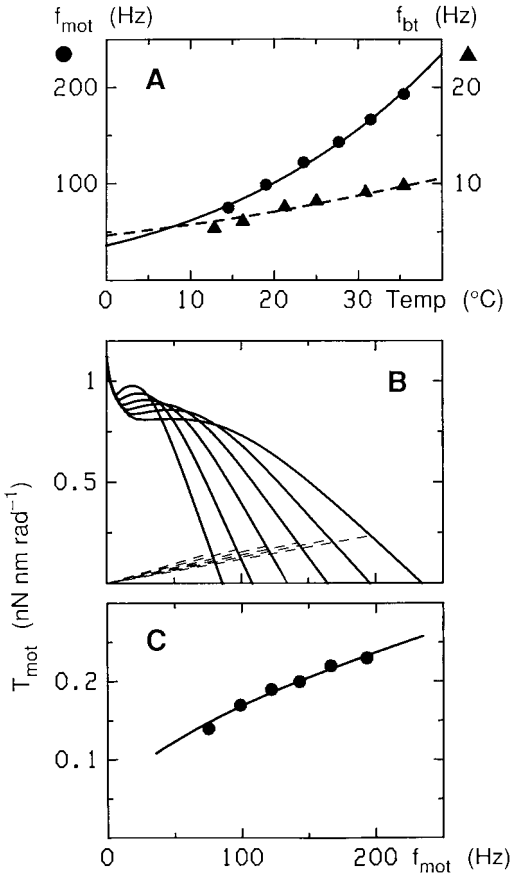

FIGURE 13 Dependence of motor frequency f_{mot} of freely swimming *E. coli* cells and body rotation frequency f_{bt} of tethered cells on temperature, as well as torque–frequency relations for counterclockwise rotation at different temperatures. (*A*) Data for f_{mot} (*circles, left ordinate*) and f_{bt} (*triangles, right ordinate*) are taken from Fig. 8 and Table 1 of Iwazawa et al. (1993), respectively; for both cases, $pH_{ex} = 7$, hence $pH_{in} = 7.43$ and $\Delta\psi_m = 125$ mV (Fig. 4 *A*). The curves represent the result of the analysis based on the model. (*B*) Simulated torque–frequency relations (*solid lines*) at 14.5, 19.0, 23.5, 27.7, 31.5, and 35.5°C (from left to right along the abscissa) using the parameter values in Tables 1 and 2. The rate constant $\alpha_{2,1}$ was calculated by means of Eqs. 42 and 43, and parameter fitting yielded the values for $\Delta G_1^{\#}(T_{ref})$ and $\partial\Delta G_1^{\#}/\partial T$ listed in the second row of Table 3. Broken lines represent frictional drags at the temperatures mentioned above. They were calculated with values of the viscosity η of the medium approximated by that of water, and with $k_{mot} = 1.67 \pm 0.03$ pN·nm·rad^{-1}·Hz^{-1}·cP^{-1} (Eq. 39) obtained from parameter fitting. T_{mot} and f_{mot} at a given temperature are determined by the intersection of the corresponding solid and broken lines. They were used to construct the curves in (*A*) and (*C*). The circles in (*C*) represent data for T_{mot} taken from Table 1 of Iwazawa et al. (1993). The lines representing frictional drag for tethered cells are not shown in (*B*) for graphical reasons; parameter fitting yielded $k_{bt} = 127 \pm 6$ pN·nm·rad^{-1}·Hz^{-1}·cP^{-1}.

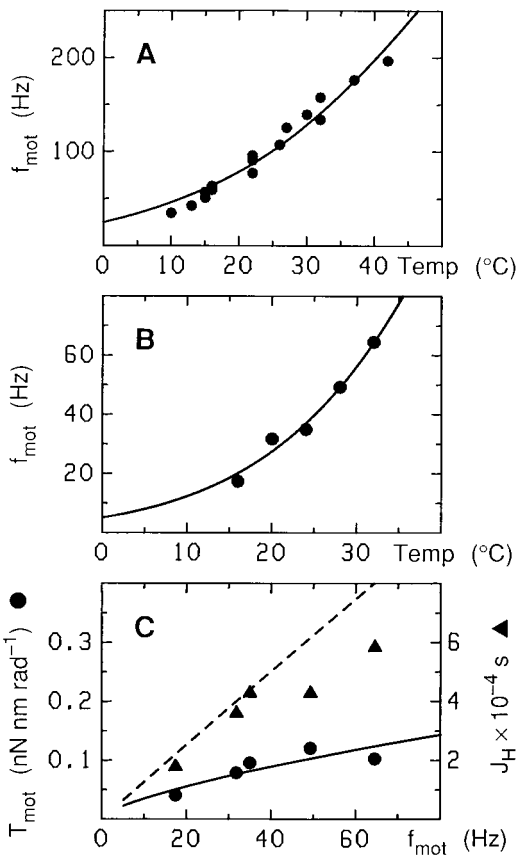

FIGURE 14 (*A, B*) Motor frequency f_{mot} of freely swimming *Streptococcus* cells as a function of temperature and (*C*) dependence of T_{mot} and J_H on f_{mot} at different temperatures. Data in (*A*) are taken from Fig. 4 of Lowe et al. (1987); $pH_{ex} = 7.5$, hence $pH_{in} = 7.5$ and $\Delta\psi_m = 132$ mV (Fig. 4 *B*). Data in (*B*) and (*C*) are taken from Figs. 3 *B* and 4 *B* of Meister et al. (1987); $pH_{ex} = 7.02$, $pH_{in} = 7.62$, $\Delta\psi_m = 45$ mV (see legend to Fig. 11 *B*). The curves represent the results of analyses performed as outlined in the legend to Fig. 13. Values thereby obtained for $\Delta G_1^{\#}(T_{ref})$ and $\partial\Delta G_1^{\#}/\partial T$ are listed in the third and fourth row of Table 3, whereas k_{mot}/(pN·nm·rad^{-1}·Hz^{-1}·cP^{-1}) $= 4.3 \pm 0.2$ and 2.5 ± 0.2, for the data in (*A*) and (*B*), respectively.

(Turner et al., 1996). In contrast, J_H is almost perfectly proportional to f_{mot} (*broken line* in Fig. 14 *C*), which validates the procedure used by Meister et al. (1987) for estimating ν_H.

The activation energies estimated for the two species under different experimental conditions are remarkably similar (Table 3). It should be noted that these data may be affected by the assumptions made in the analysis, such as the temperature independence of $\Delta\psi_m$ and pH_{in} or the approximation of the viscosity of the medium by that of water. Hence, the observed differences in $\partial\Delta G_1^{\#}/\partial T$ are most likely not significant. In contrast, the value of κ is not very crucial for the analysis. With $\kappa = 0.5$ instead of unity, the values of $\Delta G_1^{\#}(T_{ref})$ and $\partial\Delta G_1^{\#}/\partial T$ are merely reduced by 28×10^{-22} J and 0.1×10^{-22} J·K^{-1}, respectively.

Dependence on pH_{ex}

Shioi et al. (1980) have determined $\Delta\psi_m$ and pH_{in} (Fig. 4 *C*) as well as the swimming speed of *B. subtilis* for different pH_{ex} values at 30°C. It has been shown both theoretically (Washizu et al., 1993) and experimentally (Lowe et al.,

1987; Iwazawa et al., 1993) that the swimming speed v is proportional to the motor frequency,

$$v = k_v f_{mot} = k'_v f'_{mot}, \quad (44)$$

where $k'_v = k_v \alpha_{2,1}/r$. Moreover, in view of Eqs. 2, 3, and 39,

$$T_{mot} = k_{mot}\eta f_{mot} = k'_{mot}\eta f'_{mot}, \quad (45)$$

where $k'_{mot} = k_{mot}\alpha_{2,1}/r$. Because the simulations yield T_{mot} as a function of f'_{mot}, the dependence of v on pH_{ex} can be constructed as shown in Fig. 15 *A* without assigning a value to $\alpha_{2,1}$. The structural characteristics of the *B. subtilis* motor are not yet known, therefore, we have used an *E. coli* type and an *S. typhimurium* type of motor for calculating $T_{mot}(f'_{mot})$. Both yield very similar results that are in perfect agreement with the experimental data (Fig. 15 *B*).

The value $k_v = 0.228\ \mu m$ can be calculated from the data of Iwazawa et al. (1993) for *E. coli.* Using this value, we obtain $\alpha_{2,1} = 7.2 \times 10^4\ s^{-1}$ from the fitted value of k'_v, and, with this, $k_{mot}\eta = 1.9\ pN{\cdot}nm{\cdot}rad^{-1}{\cdot}Hz^{-1}$ from the fitted value of $k'_{mot}\eta$, in close agreement with the corresponding values ($7.1 \times 10^4\ s^{-1}$ at 30°C and $1.4\ pN{\cdot}nm{\cdot}rad^{-1}{\cdot}Hz^{-1}$) emerging from the analysis of the temperature dependence of f_{mot} (Fig. 13). An average value $k_v = 0.165\ \mu m$ can be calculated from the values quoted by Lowe et al. (1987) and Meister et al. (1987) for *Streptococcus.* This translates into $\alpha_{2,1}$ values of 10^5 and 1.7×10^5, and $k_{mot}\eta$ values of 1.4 and 4.7, for the *E. coli* and *S. typhimurium* types of motor, respectively. Although these values are still in line with those found in our analyses, it appears that *B. subtilis* is more likely of the *E. coli* type. In fact, the freeze fracture picture of the *B. subtilis* motor (Khan et al., 1992) closely resembles that of the *E. coli* motor.

A bell-shaped dependence of swimming speed on pH_{ex}, comparable to that shown in Fig. 15 *B*, was observed by Khan et al. (1990) for *Streptococcus* cells at room temperature. These authors have also determined the body frequency of tethered cells for pH_{ex} values between 6 and 9, and found a weaker dependence of f_{bt} on pH_{ex}. Such behavior is reminiscent of that observed for the temperature dependence and has a similar reason. Again, in a plot like that of Fig. 15 *A*, the larger k_{bt} value causes the intersections of the $T_{mot}(f'_{mot})$ curves with the straight line representing the frictional drag of tethered cells to be located at f'_{mot} values around 0.01, i.e., in the plateau region, which is less sensitive to variations in pH_{ex}.

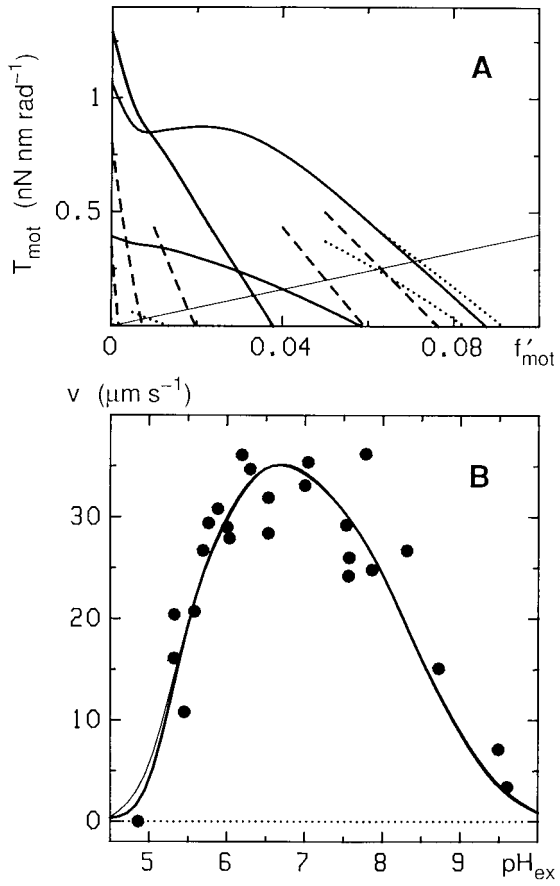

FIGURE 15 Swimming speed v of *B. subtilis* cells as a function of pH in the suspending medium at 30°C. (*A*) Torque–frequency relations $T_{mot}(f'_{mot})$ for counterclockwise rotation of *E. coli* cells, calculated with the parameter values in Tables 1 and 2. Different pH_{ex} values with corresponding values of pH_{in} and $\Delta\psi_m$ as shown in Fig. 4 *C* are indicated by different line types as follows (sequence from left to right along the abscissa): *dotted lines*, pH_{ex} = 5, 6, and 6.5; *broken lines*, pH_{ex} = 10, 9.5, 9, 8, and 7.5; *solid lines*, pH_{ex} = 8.5, 5.5, and 7. The straight line through the origin represents the frictional drag. Its intersections with the torque–frequency curves determine f'_{mot} for the pertinent pH_{ex} values (Eq. 45). These f'_{mot} values were converted to values of v (Eq. 44), which were used to construct the $v(pH_{ex})$ relation shown by the heavy line in (*B*). The thin line in (*B*) represents the result of a similar analysis but based on $T_{mot}(f'_{mot})$ calculated with parameter values pertinent to *S. typhimurium* (see Table 1). The circles in (*B*) represent data taken from Fig. 2 of Shioi et al. (1980). Parameter fitting yielded the values $k'_v/(\mu m{\cdot}s^{-1}) = 485 \pm 67$ and 544 ± 83, $k'_{mot}\eta/(nN{\cdot}nm{\cdot}rad^{-1}) = 4.0 \pm 2.4$ and 16 ± 7, for the *E. coli* and *S. typhimurium* type of motor, respectively.

DISCUSSION

Although the model described here is based on the concept proposed by Berry (1993), as shown in Table 4, it has been considerably extended and amended so that the two approaches have little more in common than the basic principle. This principle is a coupling of ion movement and rotation due to electrostatic interaction. The electrostatic interaction between a proton in a channel and the tilted alternating rows of positive and negative charges on the rotor (Fig. 1) gives rise to the free energy $G_r(\rho, z)$ for the proton (Eq. 6) as shown in Fig. 16 *A*. The free energy contributes to the activation energies that determine the rate of the transitions for protons between the binding sites in the channel (see Appendix B). The surface of *G* profiles seen in Fig. 16 *A* favors transitions into a binding site located on the floor of the valley, but represents a barrier for transitions

TABLE 4 Differences between the model of Berry (1993) and the present model

	Berry's model	Present model
(1)	Dependence of interaction energy on rotational angle approximated by a sine function (justified by reference to calculations using image forces).	Interaction energy explicitly calculated for all charges using Coulomb's law and a space-dependent dielectric constant (Fig. 16, *A* and *B*).
(2)	Effect of electrostatic interaction on proton movement between a given pair of channel sites considered for initial and final states only.	Effect of electrostatic interaction on proton movement between a given pair of channel sites considered for initial and final states, and also for the transition state.
(3)	Proton concentration included in rate constants for both binding and dissociation.	Proton concentration included in rate constant for binding but not dissociation.
(4)	Identical equilibrium constants for dissociation of protons at both ends of a channel.	Different equilibrium constants for dissociation of protons at both ends of a channel.
(5)	Intrinsic rate constants for proton transitions in a channel all set to unity.	Intrinsic rate constants for proton transitions in a channel may differ and are chosen as required by data fitting.
(6)	Array of n channels treated as an n-fold multiple of a single channel.	Array of n channels are not required to be in register with r repeat units of charges on rotor.
(7)	As a consequence of (6) electrostatic interaction between protons in different channels ignored.	Electrostatic interaction between protons in different channels taken into account.

into a binding site located on the ridge. As a consequence, the probability of the ith state, $p_i(\rho)$, tends to be centered around the minimum of the profile $G_r(\rho, z_i)$ as shown in Fig. 17 *A*, and proton movement can only occur if the binding sites are sequentially moved into the valley of the G profiles due to the rotation of the rotor.

The electrostatic interaction between a proton and the charges on the rotor gives rise to a torque $-p_i \partial G_r/\partial\theta$ (Eqs. 14). As is evident from Fig. 17 *B*, $-\partial G_r/\partial\theta$ has a maximum and a minimum of equal size for each state, and, hence, the average torque over one repeat would be zero if p_i were perfectly centered around the minimum of the profile

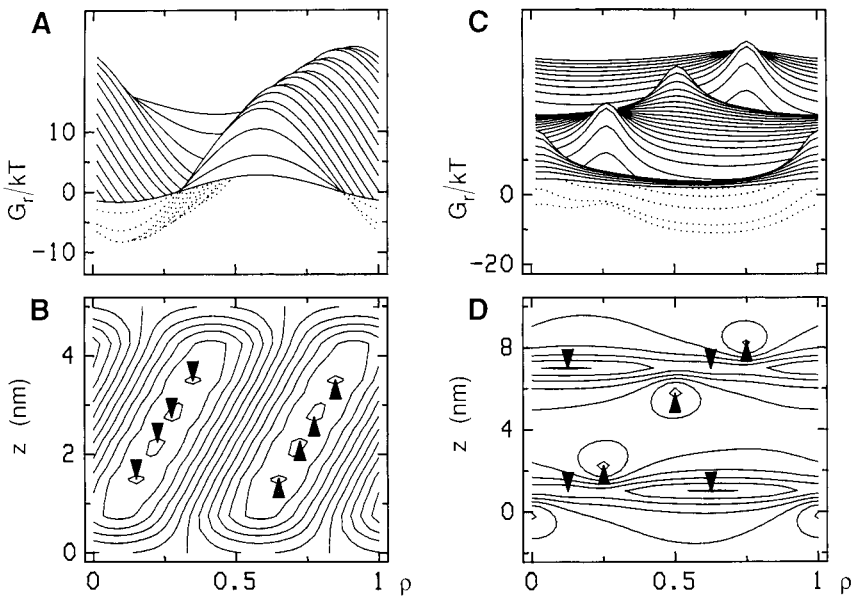

FIGURE 16 Free energy G_r due to electrostatic interaction between the charges on the rotor and a proton in a channel as a function of rotation angle and position z in the channel. (*A*, *B*) G_r was calculated from Eqs. 6 and A2–A4, using the parameter values in Tables 1 and 2, and is normalized by kT; temperature 22.6°C. The G_r surface in (*A*) is viewed at an angle of 35°; top and bottom faces are indicated by solid and broken lines, respectively. The profiles pertain to different positions in the channel, which are spaced 0.25 nm apart, and the first profile is at the channel entrance on the periplasmic side, i.e., $z = 0$ (Fig. 1 *A*). The rotation angle is expressed by ρ (Eq. 5). The contours in (*B*) indicate selected $G_r/(kT)$ values between -12 and $+12$ with an increment of 2. (*C*, *D*) $G_r/(kT)$ calculated as described by Elston and Oster (1997). Parameter values as given by the authors except for minor changes in the reciprocal electric screening distance (0.25 nm^{-1}) and the electric coupling strength (57.5 $pN{\cdot}nm^2$). Presentation as in (*A*) and (*B*) except that the first profile in (*C*) pertains to $z = -2$ nm and the values for the contours in (*D*) vary between -20 and $+10$ with an increment of 5. Upward and downward oriented arrow heads in (*B*) and (*D*) point at the positions of local maxima and minima, respectively.

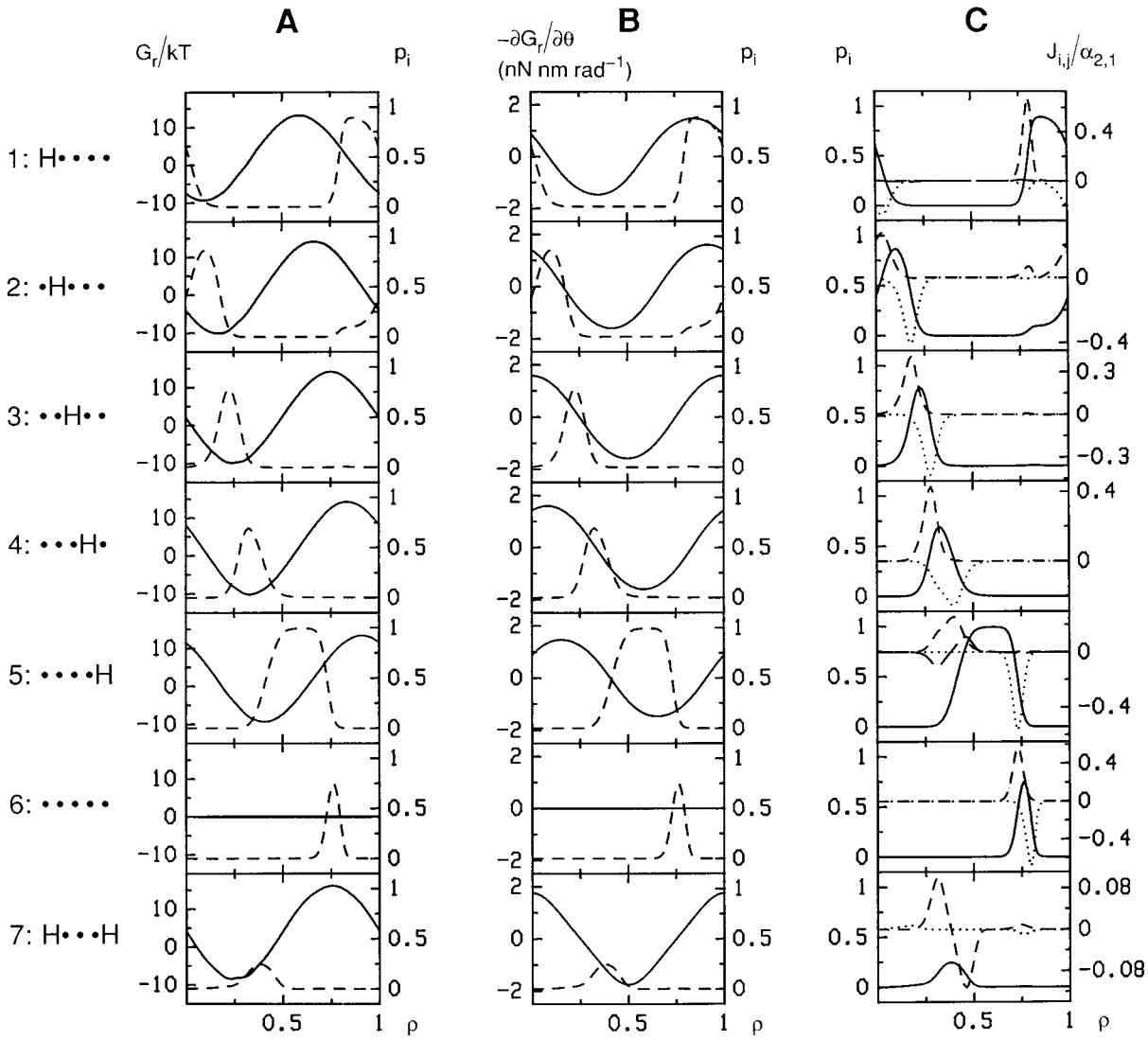

FIGURE 17 Free energy G_r of the states (*A*) and its partial derivative $-\partial G_r/\partial\theta$ (*B*), as well as flows $J_{i,j}$ between states (*C*) and probabilities p_i of states (*A–C*) at a given frequency, all as a function of rotation angle. The sequence of panels in a column from top to bottom corresponds to the numbering of states, as shown on the left (dots and H indicate empty binding sites and bound protons in a channel, respectively). The rotation angle is expressed by ρ (Eq. 5). G_r and $\partial G_r/\partial\theta$ were calculated from Eqs. 6 and 15, together with Eqs. A2–A4, using the parameter values in Tables 1 and 2. The flows $J_{i,j}$ were calculated from Eqs. 17 and 27–31, and with probabilities p_i obtained from the simulations of the torque–frequency relations shown in Fig. 9, *A* and *B*. The chosen frequency $f'_{mot} = 0.04$ is about at the end of the plateau (see inset of Fig. 18 *A*) and corresponds to $f_{mot} = 100$ and 190 Hz in Fig. 9, *A* and *B*, respectively. In (*A*) and (*B*), solid lines and left ordinates pertain to $G_r/(kT)$ and $-\partial G_r/\partial\theta$, respectively, whereas the broken lines and right ordinates pertain to p_i. In (*C*), the p_i (*left ordinates*) are represented by solid lines, whereas the normalized flows $J_{i,j}/\alpha_{2,1}$ (*right ordinates*) are represented by broken or dotted lines and are taken to indicate here flow into state *i* (that is, into state *i* when positive and out of state *i* when negative). Furthermore, the short broken and dotted lines indicate, respectively, flows between state *i* and the preceding or following states in the sense of the rotations shown in Fig. 2 *B*. The long broken lines refer specifically to $J_{5,7}$ in the case of state 5 and $J_{1,7}$ in the case of state 1. Note that $J_{1,7}$ is so small that it appears to be zero in the first panel of *C*.

$G_r(\rho, z_i)$. Because of $\Delta\tilde{\mu}_H$, this is not the case, and a net torque arises when the rotor moves through one repeat unit. Thus, the mutual effect of electrostatic interaction on proton and rotor movement causes a coupling of these two processes.

The free energy $G(\rho, z)$, which governs the transition probabilities between states, is the sum of G_r and the free energy G_c due to electrostatic interaction between the protons in the channels (see Appendix B). G_c shows little dependence on ρ and z, and its average value amounts to 2.18 *kT* for the example shown in Fig. 17. Hence, it has essentially no effect on the inner transitions and the release of protons at the channel entrances, but slows down their uptake. This effect, which is certainly present at least for the two channels within one force-generating unit, is not crucial for the behavior of our model. Similar results can be ob-

tained if the interaction between protons in different channels is neglected and the kinetic parameters ($pK_{1,ex}$, $pK_{1,in}$, G_p, $K_{i,j}$, and β_i) are readjusted, as exemplified by the broken line in Fig. 9 *C*.

The only state with multiple occupancy included in the model is that with protons in the outermost binding sites, i.e., with the largest distance between bound protons in a channel. For this case, the free energy G_p due to electrostatic interaction was determined by parameter adjustment. Its value can be interpreted in terms of Eq. A6, which yields a distance-dependent relative permittivity $\epsilon = 3.15\ \mathrm{nm}^{-1}\cdot d$ instead of $\epsilon = 8\ \mathrm{nm}^{-1}\cdot d$ (Table 2) as used when calculating the electrostatic interaction of protons with charges on the rotor or protons in other channels. The smaller proportionality constant indicates that the interior of the MotA/MotB particles is more hydrophobic. The *pK* values for binding of a second proton to a state with a bound proton situated so that they are one, two, or three sites apart are then shifted by −11.2, −2.8, or −1.25 units (22.6°C) with respect to that for an empty channel. Moreover, as may be inferred from Figs. 16, *A* and *B* and 17, the rate of binding of the second proton is slowed down due to increasingly unfavorable positions of the binding site in the G_r profiles. Hence, except for the state included in the model, states with two or even more bound protons are rather unlikely and can be neglected. This could be verified by simulations with a model including all possible states of a channel with three binding sites.

Proton movements between binding sites are represented in terms of normalized flows in Fig. 17 *C*. It is seen that protons move sequentially through the states constituting the cycle denoted by *a* in Fig. 2 *B*. The channels remain in state 5 over a relatively long ρ interval. Hence, proton uptake from the periplasmic space partially overlaps with proton release to the cytoplasm (Fig. 18 *A*). State 7 (the state of double occupancy included in cycle *b*) is reached primarily by the transitions 4 to 5 to 7, because the minimum of its G_r profile is almost at the same ρ value as that of the G_r profile of state 4. However, state 7 is also primarily depleted by the transition 7 to 5 so that cycle *b* is rarely completed. As a consequence, the second proton is bound only transiently in that it enters the channel from the periplasmic space and subsequently returns to it (Fig. 18). The probability of state 4 is almost perfectly centered around the minimum of its G_r profile and thus contributes only little to T_{mot}. In contrast, the position of the probability peak of state 7 gives rise only to a negative contribution to T_{mot} (Fig. 17 *B*). With increasing frequency, all flows increase in proportion except for those associated with state 7 (Fig. 18 *A*). Hence, the probability peak of state 7 and its negative contribution to T_{mot} gradually vanish. These features are the source of the nonlinear dependence of motor torque on frequency, giving rise to the plateaus shown in Fig. 9.

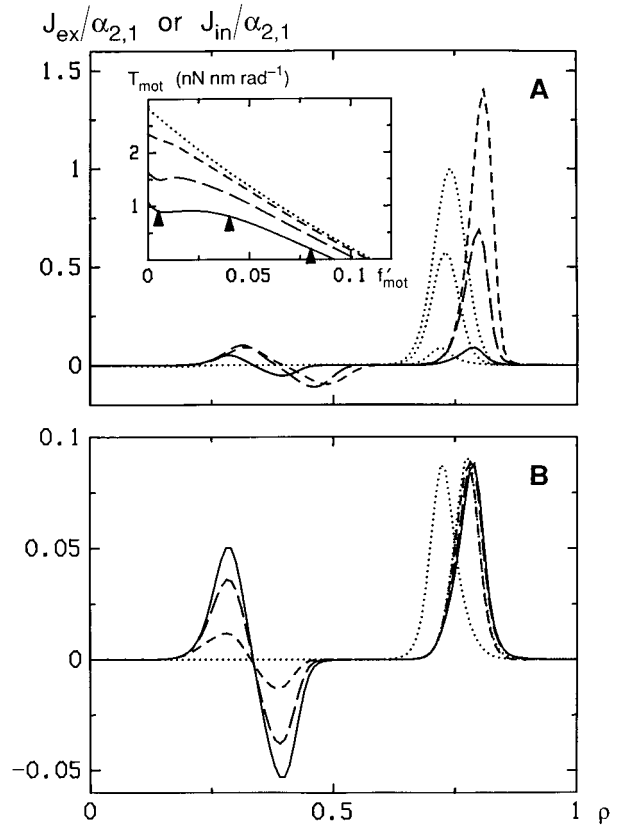

FIGURE 18 Proton flow from the periplasmic space into a channel, J_{ex}, and out of the channel into the cytoplasm, J_{in}, as a function of rotation angle. The rotation angle is expressed by ρ, as defined in Eq. 5. The flows were calculated from Eqs. 17–19 and 27–31, and with p_i values obtained as follows. (*A*) Probabilities from the simulations of the torque–frequency relations shown in Fig. 9, *A* and *B*. The frequencies chosen are f'_{mot} = 0.005, 0.04, and 0.08 (*arrow heads* in the inset), and the normalized flows $J_{ex}/\alpha_{2,1}$ are represented by a solid, a long broken, and a short broken line, respectively. The corresponding normalized flows $J_{in}/\alpha_{2,1}$ are represented by dotted lines. (*B*) Probabilities from similar simulations of T_{mot} for f'_{mot} = 0.005, but with G_p values (in 10^{-22} J) of 65.9 as in (*A*) (Table 2), 114, 222, and 939. The normalized flows $J_{ex}/\alpha_{2,1}$ are represented by a solid, a long broken, a short broken, and a dotted line, respectively. Note that the peak at $\rho \approx 0.8$, which indicates the uptake of protons from the periplasmic space, is almost identical for all cases. The dotted curve with a peak at $\rho \approx 0.7$ represents $J_{in}/\alpha_{2,1}$ for $G_p = 939 \times 10^{-22}$ J. The curves for the other G_p values (not shown) essentially coincide with it, thus indicating that the release of protons into the cytoplasm is also hardly affected by G_p. The inset in (*A*) shows the pertinent torque–frequency relations using the same line type annotation as in (*B*).

The plateaus in the torque–frequency relations are a direct consequence of the inevitable binding of a second proton due to the relatively high value of $pK_{2,ex}$, and conditions that prevent this binding should also remove the plateaus. Deliberately assigning increasingly larger values to G_p and thus decreasing $pK_{2,ex}$ (cf., Eq. B16) reduces the binding of the second proton. The plateau gradually disappears, and the torque–frequency relation approaches an almost linear dependence if binding of a second proton is

absent (see Fig. 18). On the other hand, changing the proton concentration in the periplasmic space, i.e., a variation of pH_{ex}, also affects the binding and release of the second proton. Accordingly, the plateau is most prominent around $pH_{ex} = 7$, but is considerably reduced and almost absent in the acidic and alkaline pH_{ex} range, respectively (Fig. 15 *A*). It should be added that the overall decrease of T_{mot} at $pH_{ex} = 5.5$ is not a consequence of the altered binding of the second proton, but is due to the smaller value of $\Delta\psi_m$ (Fig. 4 *C*). Our model thus predicts a clear-cut dependence of the plateau on pH_{ex} which can be challenged experimentally.

We have chosen the charge number of the channel binding sites to be zero in line with the suggestion that these sites consist of water molecules (Sharp et al., 1995). It can be shown rigorously on the basis of electrostatics that, for a given set of intrinsic rate constants, the choice of these charge numbers has no effect on the dependence of T_{tot} on rotation angle and thus on T_{mot}. However, it does change the dependence of the torque T_{ch} generated by a given channel on rotation angle (Fig. 19, *A* and *C*). Zhou et al. (1998) have recently reported that charged residues of MotA are important for torque generation. For a given set of intrinsic rate constants, such extraneous fixed charges affect the dependence of T_{ch} on rotation angle without altering T_{tot} and T_{mot} (Fig. 19, *B* and *C*), just as the charge numbers of the channel binding sites do. In addition, extraneous fixed charges co-determine the value of the intrinsic rate constants. Hence, changing them may substantially alter these rate constants so that they are no longer tuned for an optimal performance of the motor. But this effect can be assessed in quantitative terms only if more detailed information about the MotA protein is available.

Our model requires two channels per force-generating unit, which suggests two MotA/MotB complexes per unit if one excludes the possibility that two trains of water molecules interspersed between the α-helices of one MotA/MotB complex form the two channels. This is not in contradiction with experimental data because the number of complexes per unit is not yet known. In fact, structural data support this notion. If we estimate the dimension of a MotA/MotB complex with 5 α-helices (Schuster and Khan, 1994) on the basis of the electron density projection maps of the two integral membrane proteins, bacteriorhodopsin (Baldwin et al., 1988) and aquaporin-1 (Walz et al., 1995b), which, in comparison, have 7 and 6 α-helices, respectively, we find that a unit with a diameter of at least 5 nm as estimated by

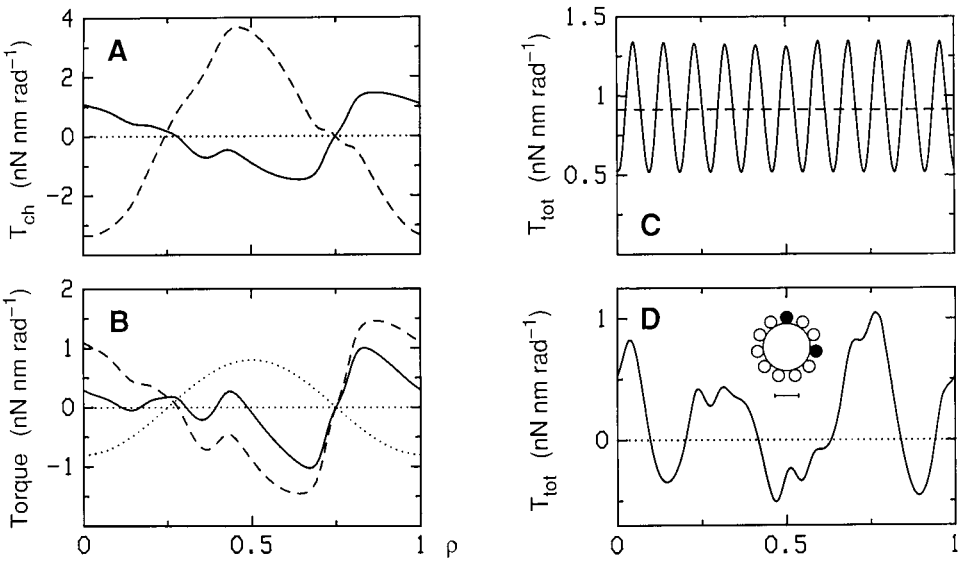

FIGURE 19 Effect of charge numbers of binding sites and of extraneous fixed charges on torque, as well as torque generated by only two units. The torque T_{ch} associated with a channel was calculated from Eqs. 14–16, and with probabilities p_i obtained from the simulations of the torque–frequency relations shown in Fig. 9, *A* and *B*. The chosen frequency $f'_{mot} = 0.005$ is just at the beginning of the plateau (inset of Fig. 18 *A*) and corresponds to $f_{mot} =$ 13 and 24 Hz in Fig. 9, *A* and *B*, respectively. (*A*) Dependence of T_{ch} on rotation angle (expressed by ρ, cf. Eq. 5) for all charge numbers Z_i of the binding sites set to 0 (*solid line*) and $Z_1 = Z_5 = 0$, $Z_2 = Z_3 = Z_4 = -1$ (*broken line*). (*B*) The torque due to extraneous fixed charges is given by $-\Sigma_j Z_j[\partial G_{r,j}/\partial\theta]_{\rho, xj, yj, zj}$. Here $G_{r,j}$ is the free energy due to electrostatic interaction between the *j*th extraneous charge and the charges on the rotor, whereas Z_j and x_j, y_j, z_j denote its charge number and coordinates, respectively. The same procedure used for protons can be used to calculate $G_{r,j}$ and $\partial G_{r,j}/\partial\theta$. It yields very similar results, and the $-\partial G_{r,j}/\partial\theta$ curves shown in Fig. 17 *B* are therefore representative also for extraneous charges. They can be approximated by sine functions, and their sum can be expressed by $A \sin\{2\pi(\rho + \delta\rho)\}$, where A and $\delta\rho$ denote an appropriately chosen amplitude and phase shift, respectively. The dotted line then represents the torque due to extraneous charges, calculated with $A = 0.8$ nN·nm·rad^{-1} and $\delta\rho = 0.5$. When added to T_{ch} for $Z_i = 0$ (*broken line*) the effective torque is obtained (*solid line*). (*C*) Total torque T_{tot} generated by all channels (*solid line*) and motor torque T_{mot} (*broken line*) according to Eqs. 20 and 24, respectively. T_{tot} and T_{mot} are identical for all cases in (*A*) and (*B*). (*D*) T_{tot} as a function of rotation angle for four channels in two force-generating units. The arrangement of the units is shown by the filled circles in the inset. The open small circles indicate the positions of the additional units in a full complement, whereas the large circle represents the rotor. The bar indicates 10 nm.

Khan et al. (1988) in freeze fracture pictures can easily accommodate two MotA/MotB complexes. Alternatively, assuming an area of about 1 nm^2 per α-helix, we find that a particle 5 nm in diameter could hold up to 20 helices. Hence, even if the diameter of the particles seen on the PF face (Khan et al., 1988) were overestimated because the particles may have the periplasmic extension of MotB still attached, there would be ample room for the 10 helices (in total) of two MotA/MotB complexes. Note also that the arrangement of the units displayed in the freeze fracture pictures shows that an equal spacing between all channels as assumed in our model is indeed possible (*inset*, Fig. 9 *D*).

We have chosen the M ring to be the rotor of the motor although some schemes suggest that the site of torque generation is at the C ring (Francis et al., 1994; Macnab, 1995, 1996). We have done so because electrostatic interaction is maximal and the membrane potential is most effective in a region of low dielectric constant. However, our model could equally well be formulated in terms of a charged ring comprising the FliG subunits located at the junction of the M and C rings (see, e.g., Fig. 4 of Lloyd and Blair, 1997). In view of the close packing of the channel complexes around the ring, the domain of electrostatic interaction would still be representable as a region of low dielectric constant. The number of charges assumed in our model to be present on the rotor can be well accounted for by the numbers of charged residues known to be present in FliG. Kihara et al. (1989) give the complete sequence for FliG, and point out that, of the 331 residues present, 95 are charged, and 26 percent of these exist in clusters of 3 or 4 adjacent residues. The actual numbers of charged residues are Asp-21, Glu-34, His-4, Lys-12, and Arg-24. This means that we can account for 36 pairs of positive and negative charges without His, and 40 including His, per FliG subunit. With the parameters chosen, each FliG encompasses 2 repeat units, so that only 12 pairs of positive and negative charges per FliG subunit are required. The remaining charges are probably sufficiently close to a charge (or charges) of opposite sign that they are essentially compensated, and hence do not act like isolated charges.

The approximations we have used when calculating the electric field are reasonable in view of the limited information currently available about the structures and conformations of the motor proteins and the MotA/MotB complexes in the force-generating units. Possible refinements would require further assumptions that cannot be justified by independent evidence, and thus would be pure speculation. In this context, it is important to note that the proportional space dependence of the relative permittivity used here is not crucial. In fact, simulations with an exponential space dependence yielded similar results in our model after appropriate readjustment of the parameter values (*broken lines*, Fig. 9, *A* and *B*). Site-directed mutations of charged residues (Lloyd and Blair, 1997; Zhou et al., 1998) have born out the importance of charges and their role in torque generation. The hypothesis presented by Zhou et al. (1998) based on such experiments is a possible mechanism depending on charged–residue interactions which, however, does not exclude or supersede our model. It has not been analyzed in quantitative terms and thus has not been proven to work as postulated. Moreover, it also suffers from the lack of detailed information mentioned above. This makes it extremely difficult to estimate the suggested effect of a variation of the ionic strength in the suspending medium on the electric field within a motor–MotA/MotB complex possessing a low dielectric constant.

It was mentioned in the section on simulation that the proteins associated with switching (FliG, FliM, and FliN) may undergo a concerted conformational change during a CCW–CW transition. This would require, in our interpretation, an alteration of the tilt angle γ by no more than 20° (from $+10°$ to $-10°$). The occasional pauses that are observed (Lapidus et al., 1988) are probably characterized by a tilt angle close to 0°. The filaments are known to have a helical structure and to undergo polymorphic transitions during switching (Macnab, 1996). Comparable changes in the basal body would be consistent with current views (Eisenbach and Caplan, 1998), and, indeed, several recent studies support this picture. For example Alon et al. (1998) have recently extended earlier considerations by Macnab (1995) and Turner et al. (1996). They consider the entire motor as an allosteric switch exhibiting concerted transitions between two discrete conformational states. This model gave a good fit to their experimental data showing fraction of time spent in the CW state versus the level of the response regulator CheY. Similar results have been reported by Turner et al. (1999).

An alternative electrostatic model has been described in considerable detail by Elston and Oster (1997). This model is based on an entirely different concept. The circumference of the rotor carries positive charges arranged on tilted rows, and the channel complex carries negative charges located on a line parallel to the rotor axis. Protons flow through a channel that is parallel to the line of negative charges but separated by a distance of 0.5 nm. This configuration gives rise to a free energy of interaction for the protons as shown in Fig. 16, *C* and *D*. It is immediately seen that, in contrast to our model, two valleys exist that run perpendicular to the channel axis. Torque is generated by electrostatic interaction between the fixed charges on the channels and those on the rotor. The role of the protons is that of a modulator in that they screen the negative charges if located appropriately. To do that, they have to cross from one valley into the next, surmounting a formidable barrier. In contrast, protons are responsible for torque generation in our model, and run along the valley floor. The only barrier to be crossed is a mild one at the exit of the channel.

Elston and Oster (1997) analyzed their model in terms of stochastic processes that included Brownian motion and, in some cases, elasticity of the anchors of the channel com-

plexes. They found that what they call the smooth-running and more restrictive steady-state occupancy approximations can significantly deviate from the stochastic result. This is demonstrated by showing probabilities, i.e., occupancies, of the states as a function of rotation angle calculated both ways. These quantities, however, have apparently been scaled by the number of classes (or bins) in the histograms and, hence, do not sum to unity. Nevertheless, they indicate that the smooth-running approximation is good in the cases considered by us, which involve the full complement of force generators. The authors modeled the frequency dependence of the relative torque obtained by Berg and Turner (1993) for tethered *E. coli* cells, the first passage statistics for *E. coli* (Samuel and Berg, 1995), and the dependence of proton flow on frequency in *Streptococcus* (Meister et al., 1987). They used identical values of the parameters for all species, some of which, however, do not correspond with current literature (e.g., radius of the rotor, external and internal pH). The agreement with experimental results is not convincing in the case of relative torque and discrepant in the case of first-passage statistics. The dependence of proton flow on frequency at low frequencies is linear but not proportional, thus indicating loose coupling, and its slope yields a stoichiometry of 105 protons per revolution, which is about 12 times too small.

Our model is highly coupled as evidenced by the proportionality between proton flow and frequency (Fig. 11). It thus supports the contention of Meister et al. (1987) that the motor is tightly coupled. A measure of tightness of coupling in linear systems is the degree of coupling (Kedem and Caplan, 1965), which is directly related to the maximum efficiency of energy conversion. Figure 20 shows examples of the efficiency of the motor calculated from our simulated behavior according to Caplan and Kara-Ivanov (1993). These examples clearly indicate that the maximum efficiency depends on conditions. The strongest effect arises from a variation of pH_{ex}, whereas an increase in temperature and a decrease of $\Delta\psi_m$ at a given pH_{ex} cause a relatively small reduction of the maximum efficiency. However, no relation between efficiency and $\Delta\tilde{\mu}_H$ seems to exist (cf., the values for $\Delta\tilde{\mu}_H$ given in the legend to Fig. 20). The degree of coupling of an equivalent linear system calculated from the maximum efficiencies amounts to 0.94, 0.85, and 0.62 for pH_{ex} = 8.5, 7, and 5.5, respectively, at 30°C. The corresponding values for pH_{ex} = 7, $\Delta\psi_m$ = 125 mV at 22.6 and 11.2°C are 0.86 and 0.88, whereas that for pH_{ex} = 7, $\Delta\psi_m$ = 0 and 22.6°C is 0.81. The variation for all other simulations at different temperatures and for different species ranges between 0.31 and 0.45 for the maximum efficiency, and 0.85 and 0.93 for the degree of coupling. Interestingly, these values are comparable to those found for mechanochemical energy conversion in striated muscle (Caplan, 1971). It is surprising that a system based on purely electrostatic interactions is capable of achieving as high a degree of coupling as one based on specific binding.

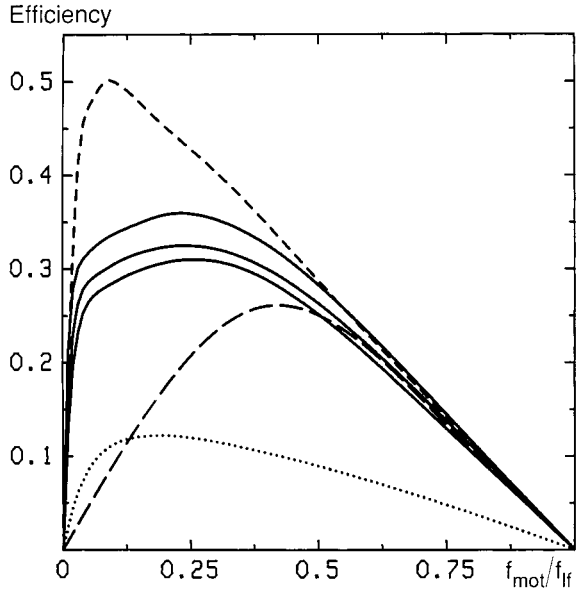

FIGURE 20 Efficiency of energy conversion between proton flow and flagellar rotation. Efficiencies were calculated as explained by Caplan and Kara-Ivanov (1993), using torque–frequency relations simulated for counterclockwise rotation of the *E. coli* motor under different conditions. Solid lines: pH_{ex} = 7, pH_{in} = 7.43, $\Delta\psi_m$ = 125 mV, temperatures 11.2, 22.6, and 30°C (*top* to *bottom*); $\Delta\tilde{\mu}_H/10^{-22}$ J = 239, 241, and 242. *Short broken line*: pH_{ex} = 8.5, pH_{in} = 7.45, $\Delta\psi_m$ = 167 mV, temperature 30°C; $\Delta\tilde{\mu}_H = 166 \times 10^{-22}$ J. *Dotted line*: pH_{ex} = 5.5, pH_{in} = 7.21, $\Delta\psi_m$ = 53 mV, temperature 30°C; $\Delta\tilde{\mu}_H = 250 \times 10^{-22}$ J. *Long broken line*: pH_{ex} = 7, pH_{in} = 7.43, $\Delta\psi_m$ = 0, temperature 22.6°C; $\Delta\tilde{\mu}_H = 40 \times 10^{-22}$ J.

The quality of our model is underlined by the fact that a large number of diverse experimental data can be simulated by a single set of chosen and adjusted parameter values. It should be noted that the window in the parameter space is rather narrow, i.e., all these parameters are crucial. Characteristic features, such as the plateau in the torque–frequency relationship or the dependence of motor torque on pH_{ex}, are lost if values outside this window are chosen. Values of parameters were deduced from structural characteristics of the motor where possible thus taking species-specific aspects into account. The values of the frictional drags emerging from the adjustment of the simulated torque–frequency relationships to the experimentally determined frequencies are reasonable and in line with the few data available from the literature. The reason for the observed large variations of $\alpha_{2,1}$ for different cells of a given species even under identical conditions is not known. However, values of $\alpha_{2,1}$ pertinent to an ensemble of cells, as well as their temperature dependence, are very similar for different species. It is worth mentioning that our model also predicts that a motor driven backwards by an externally applied torque acts as a proton pump, a feature that has yet to be demonstrated experimentally. The pumping occurs with an equally high efficiency but with a somewhat lower proton stoichiometry. This behavior, too, can be simulated with the same set of

parameter values, in contrast to the model of Elston and Oster (1997), which requires a readjustment of parameters.

We do not report here on the simulation of the effect of Brownian motion and of incomplete complements of force-generating units, but a brief mention of our preliminary findings is in place. The range of negative torques seen in Fig. 19, *A* and *B* constitutes a local impediment to rotation. However, for the ensemble of channels, these dips are to a large extent mutually compensated (Fig. 19 *C*). Simulations of trajectories $\theta(t)$ using T_{tot} and including Brownian motion of the rotor show that the remaining oscillations of T_{tot} are essentially damped out, thus giving rise to a rather smooth rotation of the motor. The analysis described by Samuel and Berg (1995) applied to these trajectories yields a linear dependence of the variance on frequency in a log–log plot with a slope of about -3. This is typical for Brownian motion in a broken motor, hence the dips of negative torque in T_{tot} cannot be responsible for the stepping of the motor described by Samuel and Berg (1995, 1996). However, this feature most probably arises from the stochastic (Poissonian-distributed) movement of protons through the small number of channels in a highly coupled system. In simulations of the so-called resurrection experiments (Block and Berg, 1984; Blair and Berg, 1988), in which MotA and MotB proteins are added serially to a motor initially devoid of them, local negative torques as seen in Fig. 19, *A* and *B* must be sufficiently small and extend over sufficiently short ρ intervals that they may be overcome by Brownian motion. We have found that, in resurrection simulations, the first observation of steady rotation occurs only after two force generators have been added in a particular configuration (Fig. 19 *D*). It is interesting that Block and Berg (1984) suggested the possibility that more than one force generator may be required for the initial rotation. In this regard, variations in channel spacing affect the behavior of incomplete complements but have a considerably smaller effect on the behavior of the full ensemble of force generators as given in Table 1. Further investigation of these issues is currently under way.

After completion of this work, a paper by Berry and Berg (1999) was published showing that the torque–frequency relationship of the *E. coli* motor is linear at frequencies up to 100 Hz in either direction. This result was obtained by taking into account the ellipticity in the rotational electric field used to exert an external torque (Berry and Berg, 1996). The parameters of our model are adjusted such that it best simulates the data considered most reliable at the time of our study. These data suggest a rising torque at increasing negative frequencies, but no real barrier against backward rotation. However, in *S. typhimurium*, the rise is not seen (Fig. 7). Preliminary simulations with readjusted parameters have shown that it is possible to obtain a more or less flat torque–frequency dependence for *E. coli* around zero frequency. To find out whether this is a reasonable solution, it would be necessary to have experimental data, determined with the new technique, that cover the full torque–frequency dependence, including the linearly declining part.

The authors propose a simplistic kinetic scheme for the mechanochemical cycle of the torque-generating units. It consists of only three states, with two transitions representing binding and release of protons on the periplasmic and cytoplasmic side, respectively, and a third transition incorporating all events which occur while the protons are within the channel. The rate constants are governed by exponentials comprising only $\Delta\tilde{\mu}_H$ and the mechanical work performed by the rotation of the flagellum. Considering the alternative ways in which the total $\Delta\tilde{\mu}_H$ and the rotational increment per proton transferred may be divided among the three transitions, the authors conclude that the best option is when all of $\Delta\tilde{\mu}_H$ and the full increment are used in the same transition, which they call a powerstroke (cf. Fig. 6 *c* in Berry and Berg, 1999). Although this model is based on oversimplifications similar to those used by Berry (1993) in his original model (Table 4), it is interesting to note that the conclusion is born out by the performance of our model. As discussed at the beginning of this section, torque is generated by the $\Delta\tilde{\mu}_H$-driven movement of the proton within the channel, and causes the concomitant turning of the rotor (Fig. 17).

APPENDIX A: ELECTROSTATIC INTERACTION ENERGIES

The free energy G of a charge with charge number Z at the position $(x_o, 0, z)$ on the channel axis (Fig. 1 *A*) due to the κth charge of the λth repeat with charge number ν, $Q_{\kappa,\lambda,\nu}$, can be calculated by means of the Coulomb potential of $Q_{\kappa,\lambda,\nu}$ and is given by

$$G = Z\nu e_0^2/[4\pi\epsilon_o\epsilon d_{\kappa,\lambda,\nu}]. \tag{A1}$$

Here, ϵ_o and ϵ are the permittivity in vacuo and the relative permittivity, respectively. The distance $d_{\kappa,\lambda,\nu}$ between the charges amounts to

$$d_{\kappa,\lambda,\nu} = [(x_o - R\cos\chi_{\kappa,\lambda,\nu})^2 + (R\sin\chi_{\kappa,\lambda,\nu})^2 + (z_{\kappa,\lambda,\nu} - z)^2]^{1/2}, \tag{A2}$$

where $x_{\kappa,\lambda,\nu} = R\cos\chi_{\kappa,\lambda,\nu}$ and $y_{\kappa,\lambda,\nu} = R\sin\chi_{\kappa,\lambda,\nu}$ have been used. The quantity $x_o = R + d_c$ is the distance between the axes of the rotor and the channel. The q charges are equally spaced on a tilted row, hence,

$$z_{\kappa,\lambda,\nu} = \kappa d_m/(q+1). \tag{A3}$$

As is evident from Fig. 1 *B*, the angle $\chi_{\kappa,\lambda,\nu}$ is related to the rotation angle θ and repeat angle ϕ by

$$\begin{aligned}\chi_{\kappa,\lambda,\nu} &= -\theta + \phi(\lambda - 1) + \chi'_{\kappa,\lambda,\nu} \\ &= \phi[\lambda - 1 + (\nu+1)/4 + P\kappa/(q+1) - \rho],\end{aligned} \tag{A4}$$

where $\chi'_{\kappa,\lambda,\nu} = \phi(\nu + 1)/4 + \delta z_{\kappa,\lambda,\nu}/d_m$, and Eqs. 5 and A3 have been used to obtain the second part of Eq. A4. The tilt angle γ (Fig. 1 *B*) is related to the pitch P by

$$\gamma = \tan^{-1}[2R \sin(P\pi/r)/d_m]. \quad \text{(A5)}$$

The free energy G of a proton at the position $(x_o, 0, z)$ on the axis of the first channel due to electrostatic interaction with the proton of the jth channel in the ith state is given by

$$G = e_o^2/[4\pi\epsilon_o\epsilon d_{j,i}]. \quad \text{(A6)}$$

The distance $d_{j,i}$ between the protons amounts to

$$d_{j,i} = [2x_o^2(1 - \cos\{2\pi j/n\})^2 + (z_i - z)^2]^{1/2}. \quad \text{(A7)}$$

For the physical significance of the parameter z_i, see Fig. 2 *C*.

APPENDIX B: TRANSITION PROBABILITIES

The standard free energy levels (Hill, 1977) for the outer and inner transitions are shown in Fig. B1. In the absence of electrostatic interaction due to the rotor charges and protons in the channels, the forward and backward transition probabilities per unit time (i.e., intrinsic rate constants) for an inner transition, $\alpha_{i,i+1}$ and $\alpha_{i+1,i}$, are determined by the standard free energy differences $G^\circ(z_i) - G^\circ(z_i^\#)$ and $G^\circ(z_{i+1}) - G^\circ(z_i^\#)$, respectively (*thick lines*, Fig. B1 *C*). The physical significance of the parameters z_i and $z_i^\#$ is illustrated in Fig. 2 *C*. Note that the standard free energies G° may include contributions from electrostatic interaction with fixed charges in the channels and/or the surroundings. In the presence of electrostatic interaction due to the rotor charges and protons in the channels, the free energy terms $G(\rho, z) = G_r(\rho, z) + G_c(\rho, z)$ (Eqs. 6 and 26) must be added to all the levels (*thin lines*, Fig. B1 *C*). This yields

$$\alpha^*_{i,i+i}(\rho) = \alpha_{i,i+1} \exp\left(\frac{G(\rho, z_i) - G(\rho, z_i^\#)}{kT}\right)\exp\left(\frac{\zeta_{f,i} e_o \Delta\psi_m}{kT}\right), \quad \text{(B1)}$$

$$\alpha^*_{i+1,i}(\rho) = \alpha_{i+1,i} \exp\left(\frac{G(\rho, z_{i+1}) - G(\rho, z_i^\#)}{kT}\right)\exp\left(\frac{\zeta_{b,i} e_o \Delta\psi_m}{kT}\right). \quad \text{(B2)}$$

The second exponential term in Eqs. B1 and B2 arises from the influence of a membrane potential $\Delta\psi_m$ on the transitions. The quantities $\zeta_{f,i}$ and $\zeta_{b,i}$ express the contributions of this potential to the forward and backward transitions, respectively,

$$\zeta_{f,i} = (z_i^\# - z_i)/d_m, \quad \text{(B3)}$$

$$\zeta_{b,i} = (z_i^\# - z_{i+1})/d_m. \quad \text{(B4)}$$

For the outer transitions involving proton binding from the periplasmic bulk phase (Fig. B1, *A* and *B*) one obtains

$$\alpha^*_{s+1,1}(\rho) = \alpha^o_{s+1,1} \exp\left(-\frac{G(\rho, z_0^\#)}{kT}\right)\exp\left(\frac{\zeta_{f,0} e_o \Delta\psi_m}{kT}\right)10^{-pH(ex)}, \quad \text{(B5)}$$

$$\alpha^*_{1,s+1}(\rho) = \alpha_{1,s+1}\exp\left(\frac{G(\rho, z_1) - G(\rho, z_0^\#)}{kT}\right)\exp\left(\frac{\zeta_{b,0} e_o \Delta\psi_m}{kT}\right), \quad \text{(B6)}$$

$$\alpha^*_{s,s+2}(\rho) = \alpha^o_{s,s+2}\exp\left(-\frac{G(\rho, z_0^\#)}{kT}\right)\exp\left(\frac{\zeta_{f,0} e_o \Delta\psi_m}{kT}\right)10^{-pH(ex)}, \quad \text{(B7)}$$

$$\alpha^*_{s+2,s}(\rho) = \alpha_{s+2,s}\exp\left(\frac{G(\rho, z_1) - G(\rho, z_0^\#)}{kT}\right)\exp\left(\frac{\zeta_{b,0} e_o \Delta\psi_m}{kT}\right). \quad \text{(B8)}$$

Here, α^o represents a second-order intrinsic rate constant (Hill, 1977; Walz and Caplan, 1995). Similarly, for the transitions involving proton binding from the cytoplasmic bulk phase one obtains

$$\alpha^*_{s,s+1}(\rho) = \alpha_{s,s+1}\exp\left(\frac{G(\rho, z_s) - G(\rho, z_s^\#)}{kT}\right)\exp\left(\frac{\zeta_{f,s} e_o \Delta\psi_m}{kT}\right), \quad \text{(B9)}$$

$$\alpha^*_{s+1,s}(\rho) = \alpha^o_{s+1,s}\exp\left(-\frac{G(\rho, z_s^\#)}{kT}\right)\exp\left(\frac{\zeta_{b,s} e_o \Delta\psi_m}{kT}\right)10^{-pH(in)}, \quad \text{(B10)}$$

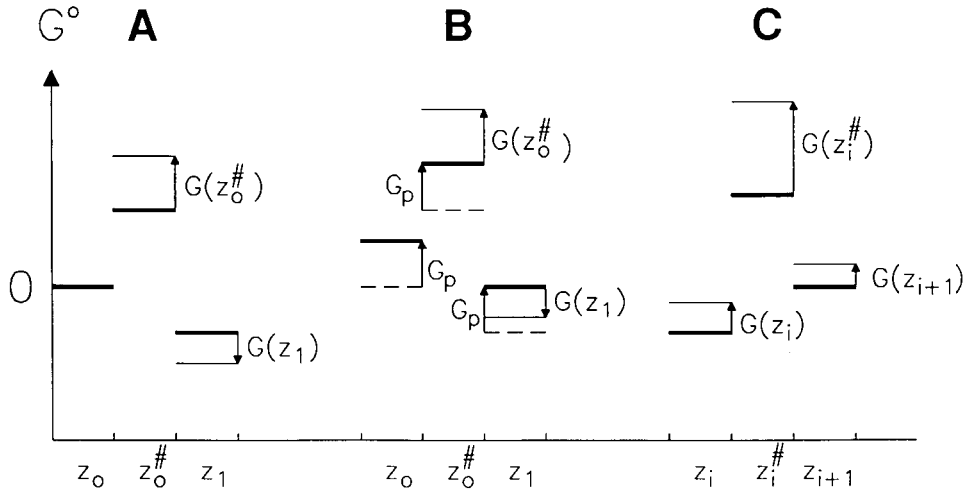

FIGURE B1 Hypothetical standard free energy levels governing proton transitions at a given value of ρ. (*A*) and (*B*) depict binding at the periplasmic entrance to a channel, (*C*) depicts a transition within the channel. The free energy levels before and after inclusion of electrostatic interactions due to rotor charges and protons in other channels (giving rise to the free energies G) are represented by thick and thin lines, respectively. The effect of prior binding of a proton at the cytoplasmic end of the channel, which, due to electrostatic interaction, shifts the levels upward by a free energy G_p, is shown at (*B*).

$$\alpha^{*}_{s+2,1}(\rho) = \alpha_{s+2,1}\exp\left(\frac{G(\rho, z_s) - G(\rho, z_s^{\#})}{kT}\right)\exp\left(\frac{\zeta_{f,s}e_o\Delta\psi_m}{kT}\right), \quad \text{(B11)}$$

$$\alpha^{*}_{1,s+2}(\rho) = \alpha^{o}_{1,s+2}\exp\left(-\frac{G(\rho, z_s^{\#})}{kT}\right)\exp\left(\frac{\zeta_{b,s}e_o\Delta\psi_m}{kT}\right)10^{-pH(in)}. \quad \text{(B12)}$$

The equilibrium constant of a particular inner transition is given by

$$K_{i,i+1} = \alpha_{i,i+1}/\alpha_{i+1,i} \quad i = 1, 2, \ldots, s-1. \quad \text{(B13)}$$

The *pK* for proton dissociation into the bulk phases become

$$pK_{1,ex} = \log[\alpha^{o}_{s+1,1}/\alpha_{1,s+1}], \quad \text{(B14)}$$

$$pK_{1,in} = \log[\alpha^{o}_{s+1,s}/\alpha_{s,s+1}], \quad \text{(B15)}$$

$$pK_{2,ex} = \log[\alpha^{o}_{s,s+2}/\alpha_{s+2,s}] = pK_{1,ex} - G_p/(kT\ln 10), \quad \text{(B16)}$$

$$pK_{2,in} = \log[\alpha^{o}_{1,s+2}/\alpha_{s+2,1}] = pK_{1,in} - G_p/(kT\ln 10). \quad \text{(B17)}$$

The second relation in Eqs. B16 and B17 arises from electrostatic interaction between the two bound protons in state $s + 2$ as expressed by the free energy G_p. Finally, thermokinetic balancing (Walz and Caplan, 1988) requires that

$$\prod_{i=1}^{s-1} K_{i,i+1} = \exp[\ln 10\,(pK_{1,in} - pK_{1,ex})]. \quad \text{(B18)}$$

Note added in proof: In a paper just published, Lloyd et al. (1999) have determined the structure of the C-terminal domain of FliG from the hyperthermophilic eubacterium *Thermotoga maritima*, and hypothesize the location and orientations of this structure in the rotor. It is interesting to note that an appropriate orientation indeed gives rise to linear arrays of alternating positive and negative charge. However, a complete structure of FliG is not yet available.

We thank Howard Berg for his very useful comments on the manuscript.

REFERENCES

Alon, U., L. Camarena, M. G. Surette, B. Aguera y Arcas, Y. Liu, S. Leibler, and J. B. Stock. 1998. Response regulator output in bacterial chemotaxis. *EMBO J.* 17:4238–4248.

Baldwin, J. M., R. Henderson, E. Beckman, and F. Zemlin. 1988. Images of purple membrane at 2.8 Å resolution obtained by cryo-electron microscopy. *J. Mol. Biol.* 202:585–591.

Berg, H. C., and S. Khan. 1983. A model for the flagellar rotary motor. *In* Mobility and Recognition in Cell Biology. H. Sund and C. Veeger, editors. DeGruyter, Berlin. 485–497.

Berg, H. C., and L. Turner. 1993. Torque generated by the flagellar motor of *Escherichia coli. Biophys. J.* 65:2201–2216.

Berry, R. M. 1993. Torque and switching in the bacterial flagellar motor. An electrostatic model. *Biophys. J.* 64:961–973.

Berry, R. M., and H. C. Berg. 1996. Torque generation by the bacterial flagellar motor close to stall. *Biophys. J.* 71:3501–3510.

Berry, R. M., and H. C. Berg. 1997. Absence of a barrier to backward rotation of the bacterial flagellar motor demonstrated with optical tweezers. *Proc. Natl. Acad. Sci. USA.* 94:14433–14437.

Berry, R. M., and H. C. Berg. 1999. Torque generation by the flagellar motor of *Escherichia coli* while driven backward. *Biophys. J.* 76: 580–587.

Berry, R. M., L. Turner, and H. C. Berg. 1995. Mechanical limits of bacterial flagellar motors probed by electrorotation. *Biophys. J.* 69: 280–286.

Blair, D. F., and H. C. Berg. 1988. Restoration of torque in defective flagellar motors. *Science.* 242:1678–1681.

Block, S. M., and H. C. Berg. 1984. Successive incorporation of force-generating units in the bacterial rotary motor. *Nature (Lond.).* 309: 470–472.

Braun, T. F., S. Poulson, J. B. Gully, J. C. Empey, S. van Way, A. Putnam, and D. F. Blair. 1999. Function of proline residues of MotA in torque generation by the flagellar motor of *Escherichia coli. J. Bacteriol.* 181:3542–3551.

Caplan, S. R. 1971. Nonequilibrium thermodynamics and its application to bioenergetics. *In* Current Topics in Bioenergetics. vol. 4, D. R. Sanadi, editor. Academic Press, New York. 1–79.

Caplan, S. R., and M. Kara-Ivanov. 1993. The bacterial flagellar motor. *Intern. Rev. Cytol.* 147:97–164.

Doering, C., B. Ermentrout, and G. Oster. 1995. Rotary DNA motors. *Biophys. J.* 69:2256–2267.

Eisenbach, M. 1996. Control of bacterial chemotaxis. *Mol. Microbiol.* 20:903–910.

Eisenbach, M., and S. R. Caplan. 1998. Bacterial chemotaxis: unsolved mystery of the flagellar switch. *Curr. Biol.* 8:R444–R446.

Elston, T. C., and G. Oster. 1997. Protein turbines I: the bacterial flagellar motor. *Biophys. J.* 73:703–721.

Felle, H., J. S. Porter, C. L. Slayman, and H. R. Kaback. 1980. Quantitative measurements of membrane potential in *Escherichia coli. Biochemistry.* 19:3585–3590.

Francis, N. R., G. E. Sosinsky, D. Thomas, and D. J. DeRosier. 1994. Isolation, characterization and structure of bacterial flagellar motors containing the switch complex. *J. Mol. Biol.* 235:1261–1270.

Fung, D. C., and H. C. Berg. 1995. Powering the flagellar motor of *Escherichia coli* with an external voltage source. *Nature (Lond.).* 375: 809–812.

Glasstone, S., K. J. Laidler, and H. Eyring. 1941. The Theory of Rate Processes. McGraw-Hill, New York.

Harvey, S. C. 1989. Treatment of electrostatic effects in macromolecular modeling. *Proteins.* 5:78–92.

Hill, T. L. 1977. Free Energy Transduction in Biology. Academic Press, New York.

Hirota, N., S. Matsuura, N. Mochizuki, N. Mutoh, and Y. Imae. 1981. Use of lipophilic cation-permeable mutants for measurement of transmembrane electrical potential in metabolizing cells of *Escherichia coli. J. Bacteriol.* 148:399–405.

Iwazawa, J., Y. Imae, and S. Kobayasi. 1993. Study of the torque of the bacterial flagellar motor using a rotating electric field. *Biophys. J.* 64:925–933.

Kami-ike, N., S. Kudo, and H. Hotani. 1991. Rapid changes in flagellar rotation induced by external electric pulses. *Biophys. J.* 60:1350–1355.

Kara-Ivanov, M., M. Eisenbach, and S. R. Caplan. 1995. Fluctuations in rotation rate of the flagellar motor of *Escherichia coli. Biophys. J.* 69:250–263.

Kashket, E. R. 1982. Stoichiometry of the H^+-ATPase of growing and resting, aerobic *Escherichia coli. Biochemistry.* 21:5534–5538.

Kedem, O., and S. R. Caplan. 1965. Degree of coupling and its relation to efficiency of energy conversion. *Trans. Faraday Soc.* 61:1897–1911.

Khan, S., M. Dapice, and I. Humayun. 1990. Energy transduction in the bacterial flagellar motor. Effects of load and pH. *Biophys. J.* 57: 779–796.

Khan, S., M. Dapice, and T. S. Reese. 1988. Effects of *mot* gene expression on the structure of the flagellar motor. *J. Mol. Biol.* 202:575–584.

Khan, S., D. Mack Ivey, and T. A. Krulwich. 1992. Membrane ultrastructure of alkaliphilic *Bacillus* species studied by rapid-freeze electron microscopy. *J. Bacteriol.* 174:5123–5126.

Kihara, M., M. Homma, K. Kutsukake, and R. M. Macnab. 1989. Flagellar switch of *Salmonella typhimurium*: gene sequence and deduced protein sequences. *J. Bacteriol.* 171:3247–3257.

Lapidus, I. R., M. Welch, and M. Eisenbach. 1988. Pausing of flagellar rotation is a component of bacterial motility and chemotaxis. *J. Bacteriol.* 170:3627–3631.

Läuger, P. 1977. Ion transport and rotation of bacterial flagella. *Nature (Lond.).* 268:360–362.

Läuger, P. 1988. Torque and rotation rate of the bacterial flagellar motor. *Biophys. J.* 53:53–65.

Lloyd, S. A., and D. F. Blair. 1997. Charged residues of the rotor protein FliG essential for torque generation in the flagellar motor of *Escherichia coli*. *J. Mol. Biol.* 266:733–744.

Lloyd, S. A., F. G. Whitby, D. F. Blair, and C. P. Hill. 1999. Structure of the C-terminal domain of FliG, a component of the rotor in the bacterial flagellar motor. *Nature (Lond.).* 400:472–475.

Lowe, G., M. Meister, and H. C. Berg. 1987. Rapid rotation of flagellar bundles in swimming bacteria. *Nature (Lond.).* 235:637–640.

Macnab, R. M. 1979. How do flagella propel bacteria? *Trends Biochem. Sci.* 4:N10–N13.

Macnab, R. M. 1995. Flagellar switch. *In* Two-Component Signal Transduction. J. A. Hoch and T. J. Silhavy, editors. American Society for Microbiology, Washington, DC. 181–199.

Macnab, R. M. 1996. Flagella and motility. *In Escherichia coli* and *Salmonella:* Cellular and Molecular Biology. F. C. Neidhardt, R. Curtiss, J. L. Ingraham, E. C. C. Lin, K. B. Low, B. Magasanik, W. S. Reznikoff, M. Riley, M. Schaechter, and H. E. Umbarger, editors. American Society for Microbiology, Washington, DC. 123–145.

McIntosh, J. E. A., and R. P. McIntosh. 1980. Mathematical Modeling and Computers in Endocrinology. Springer-Verlag, Berlin. 250–260.

Meister, M., S. R. Caplan, and H. C. Berg. 1989. Dynamics of a tightly coupled mechanism for flagellar rotation. *Biophys. J.* 55:905–914.

Meister, M., G. Lowe, and H. C. Berg. 1987. The proton flux through the bacterial flagellar motor. *Cell.* 49:643–650.

Samuel, A. D. T., and H. C. Berg. 1995. Fluctuation analysis of rotational speed of the bacterial flagellar motor. *Proc. Natl. Acad. Sci. USA.* 92:3502–3506.

Samuel, A. D. T., and H. C. Berg. 1996. Torque-generating units of the bacterial flagellar motor step independently. *Biophys. J.* 71:918–923.

Schuster, C. S., and S. Khan. 1994. The bacterial flagellar motor. *Annu. Rev. Biophys. Biomol. Struct.* 23:509–539.

Sharp, K. A., and B. Honig. 1990. Electrostatic interactions in macromolecules: theory and applications. *Annu. Rev. Biophys. Biophys. Chem.* 19:301–332.

Sharp, L. L., J. Zhou, and D. F. Blair. 1995. Features of MotA proton channel structure revealed by tryptophan-scanning mutagenesis. *Proc. Natl. Acad. Sci. USA.* 92:7946–7950.

Shioi, J.-i., R. J. Galloway, M. Niwano, R. E. Chinnock, and B. L. Taylor. 1982. Requirement of ATP in bacterial chemotaxis. *J. Biol. Chem.* 257:7969–7975.

Shioi, J.-i., S. Matsuura, and Y. Imae. 1980. Quantitative measurements of proton motive force and motility in *Bacillus subtilis*. *J. Bacteriol.* 144:891–897.

Shioi, J., and B. L. Taylor. 1984. Oxygen taxis and proton motive force in *Salmonella typhimurium*. *J. Biol. Chem.* 259:10983–10988.

Sosinsky, G. E., N. R. Francis, M. J. B. Stallmeyer, and D. J. DeRosier. 1992. Substructure of the flagellar basal body of *Salmonella typhimurium*. *J. Mol. Biol.* 223:171–184.

Turner, L., S. R. Caplan, and H. C. Berg. 1996. Temperature-induced switching of the bacterial flagellar motor. *Biophys. J.* 71:2227–2233.

Turner, L., A. D. T. Samuel, A. S. Stern, and H. C. Berg. 1999. Temperature dependence of switching of the bacterial flagellar motor by the protein $CheY^{13DK106YW}$. *Biophys. J.* 77:597–603.

Voet, D., and J. G. Voet. 1995. Biochemistry. John Wiley, New York. 349.

Walz, D., and S. R. Caplan. 1988. Energy coupling and thermokinetic balancing in enzyme kinetics: microscopic reversibility and detailed balance revisited. *Cell Biophys.* 12:13–28.

Walz, D., and S. R. Caplan. 1995. Nonequilibrium thermodynamics and kinetics. *In* Bioelectrochemistry: Principles and Practice, Vol. 1, Bioelectrochemistry: General Introduction. S. R. Caplan, I. R. Miller, and G. Milazzo, editors. Birkhäuser, Basel, Switzerland. 1–48.

Walz, D., S. R. Caplan, D. R. L. Scriven, and D. C. Mikulecky. 1995a. Methods of mathematical modelling. *In* Bioelectrochemistry: Principles and Practice, Vol. 1, Bioelectrochemistry: General Introduction. S. R. Caplan, I. R. Miller, and G. Milazzo, editors. Birkhäuser, Basel, Switzerland. 49–131.

Walz, T., D. Typke, B. L. Smith, P. Agre, and A. Engel. 1995b. Projection map of aquaporin-1 determined by electron crystallography. *Nature Struct. Biol.* 2:730–732.

Washizu, M., Y. Kurahashi, H. Iochi, O. Kurosawa, S.-I. Aizawa, S. Kudo, Y. Magariyama, and H. Hotani. 1993. Dielectrophoretic measurement of bacterial motor characteristics. *IEEE Trans. Ind. Applic.* 29:286–294.

Zhao, R., C. D. Amsler, P. Matsumura, and S. Khan. 1996. FliG and FliM distribution in the *Salmonella typhimurium* cell and flagellar basal bodies. *J. Bacteriol.* 178:258–265.

Zhou, J., S. A. Lloyd, and D. F. Blair. 1998. Electrostatic interactions between rotor and stator in the bacterial flagellar motor. *Proc. Natl. Acad. Sci. USA.* 95:6436–6441.